1-1-2010

Adaptive Radiation Therapy Of Prostate Cancer

Ning Wen
Wayne State University

ADAPTIVE RADIATION THERAPY OF PROSTATE CANCER

by

NING WEN

DISSERTATION

Submitted to the Graduate School

of Wayne State University,

Detroit, Michigan

in partial fulfillment of the requirements

for the degree of

DOCTOR OF PHILOSOPHY

2010

MAJOR: MEDICAL PHYSICS

Approved by:

_____

Advisor Date

_____

_____

_____

_____

DEDICATION

To my wife Manju Liu, for your patient, care and love to support me during the course of Ph.D. dissertation and my life. The journey is not bitter and astringent, but like sweet candy with peaceful and harmonious memory

ACKNOWLEDGMENTS

I thank my advisor Dr. Teamour Nurushev for his advice, guidance in the past five years. I really appreciate for offering me the opportunity to start my professional training at Henry Ford Hospital. His instruction, encouragement and support were invaluable in the development of this research project and my career.

Besides I want to give many thanks to Dr. Indrin Chetty for the steadfast support and insightful criticisms. He is an example to me of his precise attitude to research, dedicating to work. His supervision will be beneficial to my entire career.

Also I want to thank Dr. Jay Burmeister for the education I have at Wayne State University. It was my fortune and honor to study in this medical physics program. It was an enjoyable experience advancing through the program.

I would like to thank Dr. Harrison Guan, Dr. Jianyue Jin and Dr. Michael Joiner for the support of this project. Their expertise enriched my understanding of the subject and the context of this dissertation.

I also want to thank my colleagues, Dr. Jinkoo Kim, Dr. Hualiang Zhong, and Dr. Lei Ren. It is joyful to be working with them. Their help broadened the scope of this project.

Special thanks go to Dr. Lei Xing. His sage advice led me from the formative stages of this dissertation, to the final draft. Without his guidance and support, I could not make such progress in my research. It was wonderful experience to work with his group at Stanford University.

Most important, I deeply appreciate the sacrifice of my family during the course of my research. I owe a debt of gratitude to my wife for staying with me in the office

while I was writing the dissertation at night, for encouraging me when I was disappointed by the result, and for accompanying me in this lengthy progress. Also I want to thank my parents' endless support all the time. There is no word to express my gratitude for their love. I am lucky to have them.

TABLE OF CONTENTS

LIST OF TABLES

LIST OF FIGURES

CHAPTER 1: INTRODUCTION

1.1 Background

1.1.1 History

Radiation was applied into medicine soon after Wilhelm Roentgen discovered x-rays in 1895. The first therapeutic procedure using x-rays to treat cancer was performed within two months of the discovery. After only a few years, radiotherapy was performed throughout the United Sates for medical treatments. However, the major limitation in the early days was to produce high energy beam to treat deep seated tumors. X-rays used in the external beam radiotherapy were generated at voltages up to 300 kVp until 1950. Megavoltage beams which have energy 1MV or greater has become popular after the development of Cobalt-60 units and high energy machine like linear accelerator (Linac). There have been enormous contributions to radiotherapy from radiation oncologists and medical physicists since 1960s. Radiotherapy has become one of the primary cancer treatment techniques.

With the development of the Linac, higher energy beams can be generated to treat deep seated tumors while providing some skin sparing. Depending on tumor position and shape, single or multiple beams can be used in the planning. Up until relatively recently the patient treatment setup was done either on the therapy unit, or on a therapy unit simulator, which has exactly the same coordinate system and accessory mounts as a therapy unit, but with a diagnostic KV source in the head instead of the therapeutic MV beam, and with a provision to take scalable fluoroscopic and radiographic images or films. The

treatment fields are selected during this conventional type of simulation process. Portal films are taken from those pre-selected directions to show 2-dimensional (2D) information of the patient. The target and organ at risk (OAR) or field apertures could be drawn on the film. A hand calculation is typically performed to correlate the prescription dose to the target with the beam-on time, typically expressed as the dose rate independent Monitor Units (MU).

With CT units becoming more common in Radiation Oncology departments since the late 1980s, patient-specific volumetric information is readily available for better organ delineation and targeting. This prompted rapid development of CT-based treatment planning systems, 3-dimensional conformal radiotherapy (3DCRT) has emerged to improve tumor control while reducing dose to normal tissue by utilizing static geometric beam shaping with custom blocks or Multileaf Collimators (MLC). The conventional simulation process was replaced with a virtual simulation, based on the patient anatomical information acquired from the simulation CT scan (SIM-CT). The major difference of the SIM-CT unit and the diagnostic CT unit is in the ability to select and mark the treatment isocenter using external lasers. The treatment isocenter can be selected on-line, while the patient is still on the CT table and the corresponding alignment marks are tattooed on the patient skin. Alternatively, skin marks can be tattooed in a conventional simulation process. BB radio opaque markers are then attached to the tattoos, and the diagnostic CT is acquired and transferred into the treatment planning system. Then the corresponding treatment isocenter can be determined off-line, by localizing BBs in the diagnostic CT using the treatment

planning software. The planning flow of 3DCRT consists of setting up treatment fields based on the tumor position and surrounding organs at risk, adjusting beam shapes and weighting, adding beam modifiers like wedges or boluses, etc., calculating dose and reviewing the plan. Volumetric dose coverage (isodose lines), and, if volumes are delineated, dose volume histograms (DVH) are evaluated as a part of the plan review. If the plan is not satisfactory, the parameters can be modified and dose recalculated until an acceptable plan is achieved.

1.1.2 Intensity Modulated Radiation Therapy (IMRT)

One of the most important developments in radiation oncology is IMRT. A higher degree of dose conformality can be achieved by using IMRT. The inverse treatment planning of IMRT usually involves two steps. First the dose distribution is optimized to meet the prescription by generating fluence maps of each incident beam. Secondly, the actual fluence map is produced from the generated fluence by modulating the beam either through physical custom compensators or computer controlled MLC. The detailed procedures are described below.

The number of fields and their incident directions are set empirically by either utilizing the treatment planner's experience or appropriate treatment planning algorithms. Then a dose volume based optimization engine determines an optimal solution closest to the desired outcome based on the initial field setup. The desired outcome is usually set in the form of dose constraints and optimization functions for the target and OAR in DVH. The intensity level to each beamlet of the field and the relative weights of the fields are optimized to achieve

the goal. Ideally, planning target volume (PTV) should be covered by the prescription dose completely. However, such attempts could result in largely inhomogeneous dose distribution, especially when the PTV shape is irregular and strict constraints are placed on the surrounding critical organs. The common practice is to sacrifice PTV coverage by 2-5% to balance the normal tissue DVH and dose inhomogeneity.

Delivery of IMRT can be achieved in several ways. Custom compensators and computer controlled MLC are the two most widely used options. A compensator can be machined according to transmission values computed from a fluence pattern. If it is machined with high spatial resolution then the delivered fluence agrees with the one optimized very well. But using the physical compensators presents certain inconvenience since they need to be changed for each field manually, thus lengthening the treatment time. Also, without proper device coding and recognition, it is possible to make a mistake by putting a wrong compensator in the field. Computer controlled MLC is the most practical way to deliver IMRT. A typical MLC consists of two sets of 40-60 leaves, of various thicknesses, depending on the leaf position in the leaf bank, design and the manufacturer. The leaf sequencing algorithm calculates a series of MLC shaped apertures and a motion pattern to modulate the beam intensity according to the optimized fluence map. Depending on the correlation of the MLC movement and beam on times, the delivery can be divided into step-shoot and dynamic methods. The dynamic delivery synchronizes the simultaneous leaf

motion and radiation delivery while the step-shoot delivery separates the two instances.

1.1.3 Image Guided Radiation Therapy (IGRT)

The treatment delivery and proper positioning of the patient becomes crucial to achieve optimal delivery when using IMRT. IGRT has been increasing the accuracy of target localization using image guidance. This cutting edge innovation, combined with IMRT, improves the accuracy in delivering higher radiation doses to the tumor. Different techniques have been developed to address the tumor inter, intra fraction motion, patient setup uncertainty and geometry variation etc. Several systems are currently available commercially.

The modern Linacs like Trilogy (Varian Medical Systems, Palo Alto, CA), Synergy (Elekta AB, Stockholm, SE) or Artiste (Siemens Medical Solution, Malvern, PA) have a KV x-ray source and a flat panel imager mounted on the gantry in addition to the conventional MV electronic portal imaging device (EPID). The radiographic or fluoroscopic images can be acquired before and during the treatment using these imaging devices. It provides high contrast images to match DRR generated from planning CT with very low dose. The imaging window and level can be adjusted and filtered correspondingly for better view of certain anatomical structures. KV images are especially useful in setting up the treatment isocenter relative to bony structures or implanted fiducial markers. The drawback is it only contains 2D image without volume information and it is difficult to visualize any soft tissue.

Cone-Beam CT (CBCT) can be generated by reconstructing 300-600 projection 2D images acquired with KV or MV imagers through a range of gantry rotation. CBCT provides 3D volumetric patient information at the treatment position with good soft tissue contract to achieve precise localization and treatment setup. A 3D CBCT image can be reconstructed and viewed in minutes with fast algorithms. The use of large radiographic detectors can achieve bigger field of view coverage with high spatial resolution. CBCT can be registered to SIM-CT by matching bony anatomy or soft tissues. Couch translational and angular corrections can be performed automatically at the treatment console using couch robotics.

CT on rail is another IGRT system that has a conventional CT scanner in the treatment room that travels on two parallel rails thus allowing acquiring a 3D image of a patient in the treatment position. It shares the same couch with the Linac. The pre-treatment CT can be registered to the planning CT to correct for the daily variations in the setup and patient internal anatomy. Since it is a fan beam CT, the image quality is much better than CBCT with less scatter and shading artifacts.

Ultrasound (US) uses transducer to perform a limited scan of a patient body with high frequency sound. The returning echoes from the tissues in the body are collected by the transducer. The images are produced by identifying structures with different acoustic properties. US imaging is a noninvasive medical test without any ionizing radiation. It does not produce any radiation side effects to the patient. But US image resolution and contrast is not compatible with CT

images. Limited volume of the US image acquisition also presents challenges with defining rotational corrections.

The Calypso 4D localization system is designed to track tumor motion during the patient treatment and to perform the 3-point setup without exposing a patient to extra dose of radiation. The 3 beacon passive electromagnetic transponders are permanently implanted into specific regions of the target. Each transponder has a unique response signal which is detected by flat panel antenna array to determine the position of the target by triangulation of the signals. The system can be used for localization and tracking of target motion. It also allows adjusting the patient position continuously during radiation delivery to compensate for motion that exceeds pre-set tolerance levels.

With the implementation of IGRT, the traditional PTV margin used to account for setup uncertainties can be further reduced. Therefore, exposure to organs at risk can be reduced even further. It also improves the accuracy of targeting the tumor and opens additional possibilities for dose escalation and the next generation of treatment – Adaptive Radiation Therapy (ART).

1.1.4 Adaptive Radiation Therapy (ART)

ART can utilize daily CT or CBCT imaging to track anatomical changes, such as displacement and deformation in the target and surrounding tissues, and to adopt the treatment plan for optimal delivery accordingly. It is a closed loop system consolidating image guidance, deformable image registration (DIR), dose reconstruction, dose calculation and re-optimization. It can compensate for uncertainties related to organ deformation, inter-fraction setup errors, and

previous deviations in dosimetric deliveries. In order to implement ART clinically, there are many technical issues to be addressed, including improved image quality of CBCT, accurate dose calculation on CBCT, deformable image registration, and dose reconstruction. Also current clinical practices need to adapt the new methodology accordingly such as the optimal treatment margin for ART and cost effective schedule for reoptimization. Even though it is still in the early stages of development, ART shows the potential to be a comprehensive treatment strategy for achieving optimal radiation treatment.

1.2 Specific Aims

The goal of this investigation is to establish the framework of ART for prostate cancer treatment which is one of prevailing cancers among men in the United States. The specific aims are as follows:

a) To measure extra dose delivered to patients from daily localization using CBCT
b) To show that dose calculation on 3D CBCT image is accurate enough for treatment planning
c) To validate DIR for co-registering SIM-CT and CBCT and verify the registration accuracy
d) To compare the difference between planed and delivered doses predicted from dose deformation based on patient's geometrical variation , and its effect on tumor control and normal tissue complication using DVH and radiobiological model

e) To discuss the margin reduction and suggest an optimal margin for prostate cancer treatments after implementing ART for clinical use

f) To evaluate re-optimization schedule which balance labor intensity and ideal treatment delivery

CHAPTER 2: DOSE DELIVERED FROM CBCT TO PROSTATE CANCER PATIENTS

2.1 Introduction

CBCT using the on-board imager (OBI) device installed on a Linac allows three-dimensional (3D) online patient setup and treatment verification. Use of CBCT enables isocenter localization using soft tissue imaging, which provides a major advantage for prostate and surrounding tissues visualization on a daily basis. 2D localization based on pelvic bony landmarks using either OBI or portal imaging is less accurate (Schallenkamp, et al. 2005). In our institution, a clinical protocol has been implemented using CBCT (Varian Medical Systems, Palo Alto, CA) for daily prostate patient setup. Patients were treated to a total of 75.6 Gy in 42 fractions using the IMRT technique. Further, patients were educated about a dietary and bowel regimen to assure an empty rectum prior to simulation and treatments. If upon acquiring the CBCT during the treatment setup the rectum was found not empty or with gas, causing the displacement of the prostate or affecting the image quality, the patient was taken off the treatment table and instructed to use the restroom. A second CBCT was then acquired prior to treatment and used for localization and shifts. The accumulated total-body dose delivered from such CBCT use can be much higher than that from simulation CT and conventional EPID use. The goal of this study is to measure the daily CBCT dose.

The computed tomography dose index (CTDI) that is used to represent the diagnostic CT dose may not be adopted for the specification of CBCT dose

(CTDI is even considered less adequate for multi-slice CT scanners (Dixon 2003) (Brenner 2005). The reasons are: (1) the 10 cm long ion chamber used to measure the CTDI for diagnostic CT cannot collect all scatters from the large cone opening of CBCT; (2) the cumulative dose from CBCT may be high and the dose distribution is better measured and added to the treatment dose and (3) CBCT is quite different from diagnostic CT in terms of gantry rotational speed, bowtie design, etc. A measurement of CBCT dose has been recently reported (Islam, et al. 2006) for Elekta's Synergy system. In that study, patients' skin dose, phantom surface dose and phantom center dose (two cylindrical phantoms: 16 and 32 cm diameters) were measured at different technical settings and different field-of-views using MOSFET detectors and a Farmer chamber.

In this study, we measured the extra dose to the patients from daily localization using CBCT with standard imaging technique and fixed collimator settings. Skin doses for seven prostate patients were measured. TLD capsules were placed on the patient's skin at the central axis of three beams: AP, left lateral (Lt Lat) and right lateral (Rt Lat). In order to avoid an imaging artifact consisting of a number of concentric rings superimposed on the prostate, the treatment couch was dropped 3 cm from the patient's tattoo (i.e. central axis). This imaging artifact was fixed in the later releases of the image reconstruction algorithms. The surface doses on an IMRT phantom (CIRS, Norfolk, VA) (oval shaped: 20 cm AP and 30 cm Lat dimensions) were then measured to verify the lateral dose asymmetry noticed from in-vivo measurements on patients. A Rando pelvic phantom was used to measure the in-phantom dose distributions along the

AP and Lat central axis, including the surface doses. Phantom dose measurements were made for both the table-drop (3 cm) and central-axis setups in order to check the difference between the two. The absorbed dose was determined using the data provided by AAPM TG61 (Ma, Coffey, et al. 2001).

2.2 Materials and Methods

2.2.1 Varian's OBI system and OBI-based CBCT

Varian's on-board imager (OBI) device was installed on a dual energy 21EX linear accelerator (Linac). The OBI system consisted of a kV x-ray source (KVS) and an amorphous-silicon (a-Si) flat panel detector (KVD) in addition to the megavoltage electronic portal imaging device (EPID). The KVS and KVD were mounted on the Linac gantry via two robotically controlled arms, which position the KVS and KVD orthogonally to the treatment beam and retract when they are not in use. The x-ray tube (KVS) has two focal spots: smaller size of 0.4 mm and larger size of 0.8 mm. The x-rays can be delivered in two modes: radiographic mode and pulsed-fluoro mode. The KVD panel has a detection area of 40 cm (*X*) × 30 cm (*Y*). With the panel set at 150 cm source-to-detector distance (SDD), the maximum superior/inferior coverage is 20 cm at the isocenter plane.

OBI-based CBCT was acquired by rotating the Linac gantry from 175° to 185° in the extension mode for a total of 370° rotation. The kV source always starts from patient's Lt Lat and ends at Lt Lat resulting in a 10° over scan on the Lt Lat side. CBCT has two acquisition modes to offer two different field-of-views: full-fan mode and half-fan mode. Full-fan mode was used to scan sites where

the size is less than 24 cm (e.g., brain). KVD is centered in this mode. Half-fan mode was used for sites larger than 24 cm (mostly for body scans) and KVD was shifted to one side to cover more than half the patient's volume. Bowtie filters for either mode can be mounted to the KVS to modify the beam profile for less patient dose. Figure 1 shows a schematic of the two different modes.

Figure 1: CBCT acquisition mode. (a) Full-fan mode with full bowtie mounted. The KVD is centered with x-ray axis. (b) Half-fan mode with half bowtie mounted. The KVD is shifted to one side.

2.2.2 *Setup for CBCT dose measurement*

For all scans, a technical setting of 125 kV, 80 mA and 25 ms was used. X-rays were delivered in pulsed-fluoro mode. CBCT scans were acquired in half-fan mode using a half bowtie. In this mode, the flat panel detector was shifted to one side and the collimators were set at X1 = 5.3 cm and X2 = 24.9 cm. Y1 and Y2 were set both at 6 cm. Note that the maximum Y coverage is 20 cm at the source-to-detector distance (SDD) of 150 cm. 12 cm scan in the longitudinal

direction was a good compromise between decreasing scatter and patient overage for prostate localization.

Skin doses for seven prostate patients undergoing daily CBCT were measured. TLD capsules were placed on the patient's tattoo, i.e., the central axis of three beams: AP, Lt Lat and Rt Lat. To avoid the ring artifacts centered at the prostate, the treatment couch was dropped 3 cm from the patient's tattoo (Fig. 2(a) is the central-axis setup and 2(b) is the table-drop setup. The rings around the central axis in 2(a) moved 3 cm anterior in 2(b)). After the Lt Lat dose was found higher than the Rt Lat dose, we measured the surface doses at the same three sites on an IMRT QA phantom (CIRS model 002H9K, 30 cm× 20 cm oval shaped) in order to confirm the asymmetry. The in-phantom doses were then measured inside a Rando pelvic phantom by placing TLDs along the AP and Lat central axis; from skin to skin (therefore skin doses were also measured). The absorbed dose was determined using the data provided in (Ma, Coffey, et al. 2001). The skin and in-phantom doses were also measured for phantoms under the central-axis setup in order to check the difference to the table-drop setup. Calculation of skin and in-phantom doses were described in sections 3.4 and 3.5, respectively.

2.2.3 *The x-ray beam quality K*

For kV x-rays, the first half value layer (HVL) and kV parameters were used to specify the beam quality. The experimental setup for HVL measurement is shown in Fig. 3. Measurement was performed under the radiographic mode of OBI using a technical setting of 125 kV, 80 mA and 160 ms with a half bowtie.

High-purity (99.9%) Al attenuators were used. The Al attenuator was placed 50 cm away from a parallel-plate ion chamber (Keithly model 96035) and the x-ray collimators (blades or diaphragms) were set to 2 cm × 2 cm to make a narrow beam measurement.

The measured HVL at the central axis for a half bowtie was found to be 6.3 mm Al. For the OBI, the collimators (blades) were installed only 20 cm from the source, different from the 50 cm specification in TG61 for therapeutic KV devices. However, as long as a narrow beam was used, the default collimation setup with OBI should be acceptable.

It is worth noting that the beam near the lateral edge can be harder than at the center because of the higher attenuation by the half bowtie filter. Also, the beam spectrum near the superior/inferior beam edge is somewhat different from that at beam center (Bhat, et al. 1999). We ignore these differences in this study.

Figure 2: Dose distributions along the AP and Lat central-axis in the Rando pelvic phantom for (a) the central-axis (CA) and (b) the table-drop (TD) setups. The thin ring artifacts around the central-axis in (a) were moved 3cm anterior in (b).

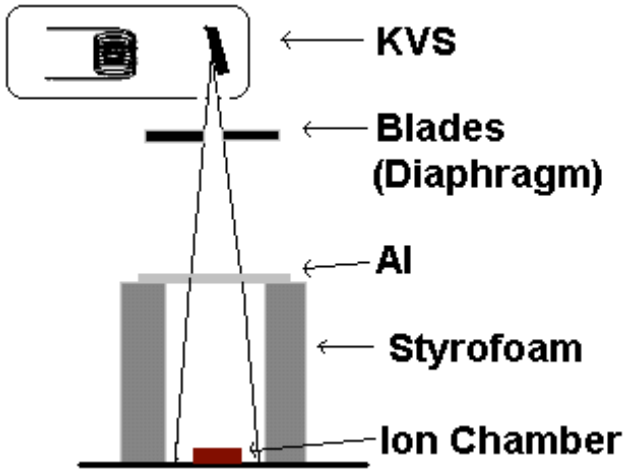

Figure 3: The experimental setup for HVL measurement.

2.2.4 *The skin (surface) dose measurement*

TLDs were used previously for the entrance surface dose (Omrane, et al. 2003) and the backscatter factor (BSF) (Coudin and and Marinello 1998) measurement of kV beams. In this study, LiF TLDs were calibrated against the Keithley parallel-plate ion chamber (model 96035) under the 125 kV x-rays with half-fan bowtie. First, the dose from KV beam was measured using the ion chamber. Then TLDs of the same batch were indexed and placed around the circle of the cylindrical sensitive volume on the surface of the parallel chamber. The sensitivity of each individual TLD was the ratio of the TLD reading to the average reading of all TLDs. Then TLDs having similar sensitivities were grouped and placed in capsules for skin dose measurement. The parallel-plate ion chamber was calibrated in an accredited dosimetry calibration laboratory (ADCL) using a 120 kV, HVL-4.15 mm Al beam and the air-kerma calibration factor N_k = 2.08×10^6Gy/C. The chamber's energy response varies <4% in a broad energy range of 20-150 KV.

The dose on patient's skin can be derived as:

$$
\begin{aligned}
D_{skin} &= D_{TLD}\left[\left(\frac{\bar{\mu}_{en}}{\rho}\right)_{TLD}^{skin}\right]_{air} \\
&= \left(\frac{R_{TLD}-R_{BG}}{R_{TLD-Cali}-R_{BG}}\right)D_{TLD-Cali}\left[\left(\frac{\bar{\mu}_{en}}{\rho}\right)_{TLD}^{skin}\right]_{air} \\
&= \left(\frac{R_{TLD}-R_{BG}}{R_{TLD-Cali}-R_{BG}}\right)D_{air}\left[\left(\frac{\bar{\mu}_{en}}{\rho}\right)_{air}^{TLD}\right]_{air}\left[\left(\frac{\bar{\mu}_{en}}{\rho}\right)_{TLD}^{skin}\right]_{air} \\
&= \left(\frac{R_{TLD}-R_{BG}}{R_{TLD-Cali}-R_{BG}}\right)MN_k\left[\left(\frac{\bar{\mu}_{en}}{\rho}\right)_{air}^{TLD}\right]_{air}\left[\left(\frac{\bar{\mu}_{en}}{\rho}\right)_{TLD}^{skin}\right]_{air} \\
&= \left(\frac{R_{TLD}-R_{BG}}{R_{TLD-Cali}-R_{BG}}\right)MN_k\left[\left(\frac{\bar{\mu}_{en}}{\rho}\right)_{air}^{skin}\right]_{air}
\end{aligned}
\qquad \textbf{(1)}
$$

Where *M* is the free-in-air parallel chamber reading after the temperature, pressure, polarity, ion-recombination and electrometer corrections; $R_{TLD\text{-}Cali}$ is the TLD reading from the calibration and R_{TLD} is the TLD reading from the skin dose measurement; and R_{BG} is the background reading of TLD. $(\bar{\mu}_{en}/\rho)_{air}^{skin}$ is the ratio of mass energy absorption coefficient of skin to air, averaged in free-air medium and it can be quoted from (Ma et al 1999, Table 2). Note that TLD's over response (~15-20%) to KV x-rays was not involved here because the effect was cancelled. In this study, skin doses for 7 prostate patients were measured and multiple measurements were made for each patient. Both the average dose and percent standard deviation (%SD) were calculated for each patient. As noted before, patient's skin dose was only measured under the table-drop (3cm) setup.

Similarly, the surface dose on phantoms can be derived as

$$
D_{skin} = \left(\frac{R_{TLD}-R_{BG}}{R_{TLD-Cali}-R_{BG}}\right)MN_k\left[\left(\frac{\bar{\mu}_{en}}{\rho}\right)_{air}^{surface}\right]_{air} \qquad \textbf{(2)}
$$

The IMRT QA phantom is manufactured from proprietary materials that fully mimic water with 1% accuracy from 50 KeV to 50 MeV and therefore $(\overline{\mu}_{en}/\rho)_{air}^{water}$ was used. The Rando phantom's soft tissue was made of a proprietary urethane formulation with an effective atomic number and mass density that closely simulates muscle tissue with randomly distributed fat. The $(\overline{\mu}_{en}/\rho)_{air}^{muscle}$ was used for dose calculation. Note that the surface dose is contributed by both the incident and transmitted projections. The effect of beam hardening for transmitted x-rays can be neglected because $(\overline{\mu}_{en}/\rho)_{air}^{muscle}$ in free-air varies <2% for all beams with HVL<10.0 mmAl. For the 30.2cmx12.0cm half-fan projection (366 cm^2), the $(\overline{\mu}_{en}/\rho)_{air}^{muscle}$ ratio is only 0.2% less than the standard 10cm x 10cm data (Ma *et al* 1999, Fig. 6). The surface doses were measured seven times for the IMRT QA phantom and four times for the Rando phantom. Measurements were made for both the table-drop (3cm) and central-axis setups.

2.2.5 *The in-phantom dose measurement*

The in-phantom doses were measured inside the Rando pelvic phantom using TLDs. The slab at which TLDs were placed has both bone and muscle-equivalent materials. TLDs were placed along the AP and Lat central-axis lines, as shown in Fig. 2(a) for central-axis setup and (b) for table-drop setup. One TLD per location and 4 measurements were made for each setup for improved dose statistics. Two or three TLD cubes were placed inside the femoral head to measure the dose to bone. Individual TLD's response was documented. Measurements were made for both the table-drop (3cm) and central-axis setups.

The in-phantom doses can be derived similarly as for Eq. (1), but the $(\overline{\mu}_{en}/\rho)$ ratio was in muscle (or bone media) but not in air. The absorbed dose inside the tissue-equivalent material is

$$D_{muscle} = (\frac{R_{TLD} - R_{BG}}{R_{TLD-Cali} - R_{BG}})MN_k\left[\left(\frac{\overline{\mu}_{en}}{\rho}\right)_{air}^{TLD}\right]_{air}\left[\left(\frac{\overline{\mu}_{en}}{\rho}\right)_{TLD}^{muscle}\right]_{muscle} \quad \textbf{(3)}$$

The $(\overline{\mu}_{en}/\rho)_{air}^{TLD}$ in free-air and in muscle (water equivalent) cannot cancel each other. However, the $(\overline{\mu}_{en}/\rho)_{air}^{water}$ in air and in water is less than 2% per TG-61 and (Ma 1999, Table 2 & 3). Taking this ~2% difference for TLD which is nearly water equivalent at 125KV, the final dose calculation can be simplified to

$$D_{tissue} = \frac{R_{TLD} - R_{BG}}{R_{TLD-Cali} - R_{BG}})MN_k\left[\left(\frac{\overline{\mu}_{en}}{\rho}\right)_{air}^{muscle}\right]_{air\ or\ water} \quad \textbf{(4)}$$

We used the $(\overline{\mu}_{en}/\rho)_{air}^{muscle}$ averaged in free-air and in water media for calculation. Similarly, the absorbed dose inside bone was

$$D_{tissue} = \frac{R_{TLD} - R_{BG}}{R_{TLD-Cali} - R_{BG}})MN_k\left[\left(\frac{\overline{\mu}_{en}}{\rho}\right)_{air}^{bone}\right]_{air\ or\ water} \quad \textbf{(5)}$$

where $(\overline{\mu}_{en}/\rho)_{air}^{bone} = (\overline{\mu}_{en}/\rho)_{water}^{bone}(\overline{\mu}_{en}/\rho)_{air}^{water}$. From (Ma *et al* 1999, Tables 2 & 3), $\overline{\mu}_{en}/\rho)_{water}^{bone}$ in free-air and in water for 6.3mm HVL beam can be ~5% different by

interpolating the data of 4.76 and 9.17 mmAl HVL. Again the average $(\overline{\mu}_{en}/\rho)_{air}^{bone}$ in free-air and in water media was used for calculation. Also the beam quality at any TLD location can be different from that used for TLD calibration in air. Based on (Ma *et al* 1999), the $(\overline{\mu}_{en}/\rho)_{water}^{bone}$ at 15 cm depth of water was 0.93 for 100 KV and 0.99 for 150 KV. We assume that for 125 KV, the ratio can be 0.96. The $(\overline{\mu}_{en}/\rho)$ bone to water ratio does not depend on SSD but field size. For the half-fan field size of 12 cm x 30.2 cm, the $(\overline{\mu}_{en}/\rho)_{water}^{bone}$ is ~2% higher than that of the standard 10cm x 10cm field.

KV dose measurements (using MOSFET detectors) inside a phantom consisting of soft tissue, bone and lung equivalent materials were reported before (Jones, et al. 2005). Based on the study, dose calculation inside bones using the free in-air $(\overline{\mu}_{en}/\rho)_{air}^{bone}$ provides ~±10% accuracy (based on the error bars) comparing to the Monte-Carlo simulation. Considering TLDs have less energy response than MOSFET, we expect the inaccuracy of bone dose calculation due to the approximation in Eq. (5) was better than 10%.

2.3 Results

2.3.1 Skin dose on patients (table-drop setup)

Table 1 showes the average skin doses and the percent standard deviations (%SD) at AP, Rt Lat and Lt Lat for patients of different sizes. The number of measurements (trials) was also given for each patient. AP dose strongly depends on patient's separation, ranging from 3.2 cGy for 32.7 cm to 6.1 cGy for 20.5 cm. Lat doses had little dependence on patient's separation. Rt Lat

dose was 2-3 cGy, which was lower than the Lt Lat dose of 3.5-4 cGy by about ~40%. The standard deviations range from 3.5% to 17% for all data.

The fact that large patients received less AP doses is because of less transmission from posterior and posterior oblique projections, despite that large patients actually received higher skin doses from anterior and anterior oblique projections (because of the shorter source to skin distances, or SSD). For the three patients with AP separations 23.74 cm, 25.46 cm and 27.18 cm, AP doses were actually increased a few percent with increased separation. This means that the increased entrance doses from anterior projections outweigh the decreased transmission from posterior projections. For very thin (<22 cm) patients, the increased transmission outweigh the decreased entrance dose.

Table 1. AP and Lat skin doses for patients (Table drop setup)

Patient	Total Trials	TLDs Each Trial	Patient Separation		AP Dose		Rt Lat Dose		Lt Lat Dose	
			AP (cm)	Lateral (cm)	Average (cGy)	%SD	Average (cGy)	%SD	Average (cGy)	%SD
A	4	20	32.65	40.24	3.22	5.51%	2.68	8.75%	3.94	9.10%
B	5	20	27.18	40.07	4.54	7.75%	2.55	11.27%	4.12	8.52%
C	3	20	25.46	38.56	4.29	6.77%	2.54	6.23%	N/A	
D	5	20	23.74	37.28	4.10	8.73%	2.39	3.46%	3.49	6.25%
E	6	20	22.77	34.91	5.05	8.93%	2.51	5.95%	4.25	3.77%
F	6	20	21.7	36.04	6.02	3.78%	2.34	7.06%	N/A	
G	7	20	20.48	34.16	6.06	10.82%	2.78	16.78%	N/A	

2.3.2 Surface dose on phantom

Table 2 first showed the surface doses and percent standard deviations (%SD) at the same three sites on the IMRT QA phantom for both the central-axis (CA) and table-drop (TD) setups. For this exactly symmetrical phantom, Lt Lat doses were measured to be ~40-50% higher than the Rt Lat doses. Comparing the table drop setup to the central-axis setup, AP dose was increased a few

percent but Lt Lat and Rt Lat doses were each decreased by a few percent. The surface doses on the Rando pelvic phantom at the same three sites were also measured (at the time for in-phantom dose measurement) and shown on the second row of Table 2. With table-drop, AP dose is also increased in this case (may because that more side projections become incident rather than transmitted, which offset the dose decrement from the larger anterior SSD) but the Lt Lat and Rt Lat doses changes little.

Table 2: Phantom surface doses from the central-axis (CA) and table-drop (TD) setups

Phantom	Num. trials	TLDs per trial	Sep. (cm)		CA (SAD=100cm) (cGy)						TD (SAD=103cm) (cGy)					
					AP		Lt Lat		Rt Lat		AP		Lt Lat		Rt Lat	
			AP	Lat	Ave	%SD	Ave	%SD	Ave	%SD	Ave	%SD	Ave	%SD	Ave	%SD
IMRT	7	25	20	30	4.73	5.71%	4.52	4.23%	3.00	5.35%	5.12	4.31%	4.13	2.89%	2.77	2.92%
Rando	4	25	20	33	4.91	4.83%	4.21	3.65%	2.61	3.47%	5.73	3.89%	4.30	4.03%	2.83	3.66%

2.3.3 In-phantom dose in phantom

The in-phantom doses measured inside the Rando pelvic phantom using TLDs, along the AP and Lat central-axis (tattoo) were shown in Fig. 2 for (a) the central-axis and (b) the table-drop setups. The results were the average of all 4 measurements for each setup. Again, the tissue and bone doses on the left side were higher than those on the right side. The anterior part of the phantom also received higher doses with table drop than with the central-axis setup. Doses at the AP, PA and Lt Lat peripheral area (except at the Rt Lat where the dose is about the same as the central dose ~3 cGy.) were ~40-50% higher than at the central. The left femoral bone received the highest doses of 10-11 cGy while the right one received ~6-7 cGy.

2.4 Discussion

More measurements were made later in half-fan or full-fan scan, with or without bowtie, central-axis or table drop setup and all confirmed that the Lt Lat dose was higher than the Rt Lat dose. This dose asymmetry was found due to: (1) KV source always starts from Lt Lat and ends at Lt Lat. Gantry rotation get much slower near the end but dose rate stays constant; and (2) 10 deg scan overlap on the Lt Lat side (start and end). In-phantom dose measurement also confirmed that the peripheral dose at AP, PA and Lt Lat is higher than the central dose by about ~40%. The Rt Lat dose is about the same as the central dose.

The normal tissue integral dose for a total of 42 fractions is in the range of ~130 (central) to 200 (skin) cGy. Despite this dose is only ~2% of the prescription dose; it is, however, distributed over the whole scanned volume. Particularly, dose at the left femoral head can be up to 11 cGy per scan and the total dose can be more than 400 cGy from the whole treatment course. Adding this dose to the femoral dose received from treatment beams, which is ~3400 cGy in our institution, the total dose is still under tolerance (beam quality at 125 KV is close to that at MV.) However, the advantage of CBCT guided RT versus the disadvantage of additional KV dose may need further investigation, especially if low KV is used in the future. On the other hand, it is not too difficult to consider the CBCT dose as part of the prescription dose. Previously a model-based treatment planning system was developed for dose computations in the KV energy range using ADAC's Pinnacle system (Alaei, Gerbi and Geise, Evaluation of a model-based treatment planning system for dose computations in the

kilovoltage energy range, 2000). It used the Monte Carlo technique to generate photon energy deposition kernels (Alaei, Gerbi and Geise, Generation and use of photon energy deposition kernels for diagnostic quality x-rays, 1999). The system was already applied for lung dose calculation at KV x-rays (Alaei, Gerbi and Geise, Lung dose calculations at kilovoltage x-ray energies using a model-based treatment planning system, 2001) and it could be used for the calculation of KV dose from CBCT.

The current Varian's CBCT used a total of 1320 mAs (660 projections, 2 mAs per projection, 125 KV). Compared to the total 660 mAs (330 projections) used in Synergy system at 120 KV, Varian's CBCT delivers approximately doubled dose. For Synergy system (Islam 2006), the doses at the center and the surface for a cylindrical phantom of 30 cm diameter were 1.6 cGy and 2.3 cGy, respectively, which were about half of our measurement. Also, the lateral dose asymmetry was not reported for the Synergy system. By evaluating the image quality versus the number of projections for clinical needs, the number of projections for Varian's CBCT may be reduced as well despite that the current CBCT used fixed projection number and technical settings. Some dose reduction strategies as discussed in (Islam, et al. 2006) could also be used for Varian's CBCT.

2.5 Conclusion

Absolute dose measurements have been made for pelvic CBCT scans with fixed technical and collimation settings using TLDs. These include skin doses for real patients and surface in-phantom doses for phantom. There were

two major findings from the measurements: (1). the lateral dose distribution is not symmetrical, with Lt Lat being ~40% higher than Rt Lat and (2). AP skin dose varies with patient size, ranging 3.2-6.1 cGy for patient's AP separation of 20-33 cm (the larger the separation, the less the skin dose) but lateral skin doses depend little on separations (Lt Lat dose was ~4.2 cGy and Rt Lat dose was ~2.6 cGy in average). The in-phantom peripheral doses at AP, PA and Lt Lat areas were higher than the central dose (~3cGy) by about ~40% but the Rt Lat dose was about the same as the central dose. The highest in-phantom dose was inside the left femoral head (neck/hip joint region) where the maximum dose can be up to 11 cGy. The CBCT dose delivered to pelvic site for a total of 42 fractions can range from ~130 cGy to the central tissue, ~200 cGy to most of the peripheral tissues, and more than ~400 cGy to the left femoral bone. Varian released a new OBI version 1.4, which promised to reduce the CBCT dose. Several studies have been done to measure the absorbed dose from CBCT (Palm, et al. 2010) (Ding, et al. 2008). The CBCT dose is significant lower in the default CBCT modes with OBI 1.4 for pelvic scan (pelvis or pelvis spot light). However, the image quality and spatial resolution has been compromised to lower the dose.Varian released a new OBI version 1.4, which promised to reduce the CBCT dose. Several studies have been done to measure or use Monte Carlo simulaton to calculate the absorbed dose from CBCT (Palm, et al. 2010) (Ding, et al. 2008). The CBCT dose is in OBI 1.4 can be reduced to one-fifth of the dose received with OBI 1.3 for head and neck region while the dose can be halved in the pelvic scan. The default CBCT modes in OBI 1.4 for pelvic scan are pelvis

spot light (125kV, 80mA, 25ms) and pelvis (125kV, 80mA, 13ms). The pelvis spot light acquires CBCT images in 200 degrees acquisition angles instead of 360 degrees. CBCT dose in the pelvis mode is reduced due to lower mAs. The image quality and spatial resolution has been compromised to lower the dose in OBI 1.4. The advantage of CBCT guided RT versus the disadvantage of additional KV dose worth to be further investigated.

CHAPTER 3: ADAPTIVE RADIATION THERAPY

3.1 Introduction

Radiation beam can be controlled and shaped to the TV precisely under the development of modern linear accelerator and MLC. The advancement of IMRT allows modulating the intensity of the beam to further improve the dose conformality to the target and to minimize the dose to surrounding critical organs.

However, the level of precision achieved in the plan may not be applied to the real world. The intra- and inter- fraction motion can potentially negate the merit of IMRT. The expansion from clinical target volume (CTV) to planning target volume (PTV) accounts for internal organ motion and setup errors. The method significantly compromises the effectiveness of IMRT. IGRT is emerging by using different imaging modalities to assess the real time patient geometry and applying shift to match planning position. CBCT is one of the imaging tools to provide online patient setup information to correct for inter-fraction motion. The online matching algorithm used in KV CBCT system is rigid body registration which has six degrees of freedom (three translational and three rotational). The online table correction can be done either 4D (Exact couch) or 6D (robotic couch) based on the registration results. However, the studies have shown that the position and shape of the TV and OAR vary between the simulation and treatment, which may have consequences of impacting tumor control and normal tissue complication probability (Pollack, et al. 2002) (Roeske and al. 1995) (Beard, et al. 1996) (Tinger, et al. 1998) (Dawson, et al. 1998) (Zelefsky, Crean,

et al. 1999). Such anatomy deformations are also observed in our daily clinical practices which bring difficulty to apply IGRT effectively (Fig.4).

Figure 4: Anatomy deformation is shown between SIM-CT (left upper corner) and three treatment sessions. Rectal gas increases the rectal volume and causes the movement and deformation of prostate.

The patient anatomy and positioning information obtained from CBCT allow us to assess the anatomy deformation and dosimetric implications and make corrections during the course of treatment. With 3D volume information, CBCT offers the opportunity to elevate radiotherapy to the next level – ART.

ART is a closed-loop feedback algorithm which evaluates the organ deformation and motion right before the treatment and takes into account dose delivery variation daily to compensate the difference between planned and delivered dose. It also has a potential to allow further dose escalation and margin reduction to improve the clinical outcome. A serious of studies has shown that

dose escalation can improve the outcome of treatment of prostate cancer (Zelefsky, Leibel, et al. 1998) (Pollack, et al. 2002) (Peeters, et al. 2006) (Martinez, et al. 2005). ART is the promising strategy to optimize the delivered dose distribution to both the target and OAR.

3.2 Materials and Methods

3.2.1 Image-Guided Radiation Treatment of prostate cancer

An institutional review board (IRB) approved protocol has been established at Henry Ford Hospital to evaluate various IGRT modalities in prostate cancer treatment. All the patients enrolled in the protocol were instructed for the bladder and bowel preparation. The patient position and rectum/bladder filling were assessed during the CT simulation by acquiring a short length helical CT scan. The full bladder and empty rectum without gas were required for planning purpose. The patients were simulated in 3 mm slice thickness with Brilliance CT 16-slice (Philips Medical Systems, the Nederland). No Intravenous or oral contrast was given to the patient. The technical settings of the pelvis protocol were 120kV, 500mAs. The prescription dose for most patients was 75.6Gy (1.8Gy x 42 fractions). If the patient was also under the IRB gene therapy protocol then 80Gy (2Gy x 40 fractions) was prescribed based on the criteria of the protocol. The CTV included prostate and 1cm proximal seminal vesicles which were defined as the geometrical intersection of seminal vesicles with prostate expanded by 1cm margin. PTV was created by adding 1cm margin to CTV except 6mm posteriorly to limit rectal dose. The treatment plans were 7 to 9 fields IMRT (Fig.5.).

There is a normal tissue dose constraint criteria used at Henry Ford Hospital for treatment planning. This criterion matches the normal tissue dose/volume tolerance guidelines published recently by the Quantitative Analysis of Normal Tissue Effects in the Clinic (QUANTEC, Lawrence, et al. 2010). The comparisons of the two guidelines for rectum and bladder are listed in table 3. All the treatment plans optimized under Henry Ford criteria are also evaluated to comply with the QUANTEC guideline.

Table 3: OAR constraints criteria for prostate cancer treatment

	Volume	10%	15%	20%	25%	30%	35%	40%	50%	60%
HF Criteria	Rectum	75	-	70	-	65	-	60	-	40
	Bladder	80	-	75	-	70	-	65	-	45
Quantec	Rectum	-	75	70	65	-	60	-	50	-
	Bladder	-	80	-	75	-	70	-	65	-

Figure 5: 9-fields IMRT treatment plan of prostate cancer.

CBCT was acquired before each treatment for online image guidance. The rigid registration was performed online to fuse CBCT to SIM-CT. After the scan was completed, SIM-CT and CBCT were further processed in the 3D/3D match workspace for the co-registration and anatomy evaluation. The CBCT images were evaluated first. If the bladder or rectum fillings were not satisfactory for the treatment, the patients were taken off the treatment couch and instructed to drink more water, void the bladder and rectum or otherwise achieve better condition. After the patient has followed the instructions, he would be re-positioned on the treatment couch and another CBCT was re-acquired. The final CBCT and SIM-CT image data sets were then matched using automatic image registration algorithm with four degrees of freedom as shown in Fig.6 (three translations and one couch rotation). If the auto registration did not match the images well, the

registration could be adjusted by manual matching. The patient position was corrected in three translational directions based on registration results.

Figure 6: Online 3D-3D rigid image registration of SIM-CT and CBCT.

Five patients were selected to be processed retrospectively for this ART study. The maximum CBCT longitudinal scan range was about 20cm when source to detector distance was 150cm which was the standard clinical setting. However, the reconstructed 3D information was shorter due to the loss of information at the peripheral region. If the lymph node was involved in the treatment, CBCT could not cover all the treatment area. Therefore, there was not enough information to reconstruct the dose and re-optimize the calculation. Only

low risk patients with localized prostate cancer were selected for the study (table 4). The risk classification was defined as following:

Low risk: prostate cancers are unlikely to grow or spread for many years

- PSA<10ng/ml
- Gleason score <=6
- Stage: T1 and T2a

Intermediate risk: cancers are unlikely to grow or spread for a few years

- PSA is between 10 and 20 ng/ml
- Gleason score is 7
- Stage: T2b and T2c

High risk: cancers may grow or spread within a few years

- PSA >20 ng/ml
- Gleason score is 8 - 10
- Stage: T3 and T4

Table 4: The patients' prognostic factors and treatment plan parameters

Patient	1	2	3	4	5
Age	65	78	64	78	61
CTV (cc) **(Prostate+1cm Prox SV)**	63.27	51.2	32.19	69.64	48.23
PTV definition	1cm around 6mm posterior	1cm around 4mm posterior	1cm around 6mm posterior	1cm around 6mm posterior	1cm around 6mm posterior
PSA (ng/ml)	3.3	5	3.23	7.9	5
Gleason Score	6	7	6	6	6
T stage	T1c	T2	T1c	T2	T1c
Dose Fraction	42	40	42	40	42
Prescription Dose (Gy)	75.6	80	75.6	80	75.6

3.2.2 CBCT based dose calculation

3.2.2.1 HU (hounsfield unit) number – relative ED (electron density) calibration

CBCT has great potential to be used for the ART better than other image modalities since it has the quantitative advantage as CT images and volumetric information of patient online position. However, scatter and artifacts in the current CBCT images degrades its application in target delineation and dose calculation. The dose calculation accuracy needs to be carefully evaluated before its

implementation in ART. Several studies have demonstrated the feasibility of using CBCT for dose calculation (Ding, et al. 2007) (Yoo and Yin 2006). Since the accuracy of CBCT based dose calculation is vital for ART, the dosimetric feasibility of CBCT was re-evaluated.

The scatter contribution of CBCT was proportional to scan volume. Guan (Guan and Dong 2009) recommended the HU-ED calibration should be done for each scanning mode. Since the study only focused on ART of localized prostate cancer patients with same CBCT scanning parameters, the ED-HU calibration was evaluated for the pelvis setting only. In the pelvis mode, the technical setting of CBCT was 125 kV, 80mA, 13ms and the scan was performed in half fan mode with half bow-tie mounted. The blade size Y was set to 12cm symmetrically for all patients.

The Catphan 500 (The Phantom Laboratory, Salem, NY) is the standard phantom for CBCT calibration. It has five different modules for CT QA. CTP404 module consists of seven high contrast sensitometric targets which are made from Teflon®, delrin®, acrylic, polystyrene, water, low density polyethylene, PMP and air. The CT numbers for these targets range from -1000 to 1000. The phantom and one axial slice of the phantom are shown in Fig. 7. The phantom was scanned in both SIM-CT and CBCT under the standard clinical settings for the pelvic site. HU for each target was measured by averaging the value of 10 points surrounding the center of the target (Fig.7).

Figure 7: (a) Catphan 500. The diameter and length of the phantom are both 20cm. (b) The SIM-CT axial slice and (c) the CBCT axial slice of Caphan which show eight targets for HU-ED calibration.

3.2.2.2 Dose calculation evaluation – phantom & patient study

The Rando Pelvic phantom was used to evaluate the accuracy of dose calculation of CBCT. The Rando phantom was scanned in both SIM-CT and CBCT and the two image sets were co-registered in Eclipse. The structures were drawn to represent prostate, bladder and rectum in SIM-CT and copied to CBCT. There was minor difference (< 1%) of the volumes in the two image sets due to interpolation since the pixel matrix is different between SIM-CT (512x512) and

CBCT (384x384). The treatment plan was calculated using 6MV beam in the Eclipse treatment planning system with pencil beam algorithm. There were three different treatment plans used for the evaluation, 4-fields box with / without inhomogeneity correction and 9 fields IMRT. 4-fields box was the 3D plan to treat pelvis using AP, PA, Lt Lat, and Rt Lat beams. It provided a relatively high dose box at the intersection of the beams where the lesions were located. The 9-fields IMRT plan was generated from the standard template used for the prostate cancer treatment at Henry Ford Hospital. The gantry angles were 200°, 240°, 280°, 320°, 0°, 40°, 80°, 120°, and 160° respectively. The optimization was based on the same criteria (table 7). Modified Batho method was used for the inhomogeneity correction. All three plans were generated in the SIM-CT and copied to the CBCT to recalculate with same beam parameters.

Same method was applied to study the dose calculation accuracy for patients. One CBCT image set of a patient with minimum organ deformation compared to SIM-CT was chosen for evaluation. The CBCT image was registered rigidly to the SIM-CT in Eclipse. All the structures were duplicated to the CBCT image set. The original plan used for the patient treatment was copied and re-calculated on the CBCT image set.

3.2.3 Deformable Image Registration (DIR)

The image uses voxels to sample a continuous field. Each voxel is monochromatic and has same size in any particular image. Each voxel has x, y and z dimension and intensity associated with it. The finer the voxel is, the more accurately it represents the original image. The greater the bit depth is, the better

the contrast resolution. All the voxels are indexed in the image grid (Fig.8). Image registration transforms the points in one image to the corresponding points in the other image. However, such transformation cannot be converted from one image grid to the other image grid directly. It needs to be transformed in the physical coordinate and converted back to the image grid (Fig.9). The voxel physical coordinate along each direction is defined as

$$V[n] = Origin + Index[n] \times size \quad \textbf{(6)}$$

Figure 8: The grid samples the continuous image. All the voxels laid on the grid are indexed. The typical voxel matrix in the CT image is 512 x 512 x 3 and the bit depth is 16 bits. The voxels are indexed in all three dimensions. The voxel sizes in x and y dimension are calculated by field of view/matrix size and the voxel size in z dimension is equal to slice thickness.

Figure 9: The image registration cannot be performed on the image grid directly. The physical coordinates of the pixels in the fixed image are calculated based on the image origin, pixel index and size. The pixels are transformed from physical space of fixed image to that of moving image. Then the moving image is resampled.

There are two different objects in the image registration, fixed image and moving image. The moving image is the one to be re-sampled back to the fixed image grid. Denomination of the fixed/moving image is arbitrary. However, since CBCT contains the patient anatomy information at the treatment position, doses should be calculated on CBCT and warped back to SIM-CT for post processing and composite dose summation. Because doses are reconstructed in the opposite direction of the vector fields that define the mapping from the fixed image to the moving image, the fixed image should be SIM-CT and the moving image should be CBCT acquired from each treatment session. The correct image voxel size and origin is vital for registration since it is done in the physical coordinates. The comparison of image coordinate between CBCT and SIM-CT is

listed in table 5. All the DICOM images are converted into 3D raw data for the registration. The header of the raw data should specify image coordinate and bit depth information in order to register accurately in the physical coordinates.

The purpose of image registration is to maximize the similarity metrics between the fixed image and the moving image through transformation. Rigid registration only allows 6-degrees of freedom of transformation. All the voxels move along the same direction with the same quantity. It is not sufficient for accurate registration which can account for organ deformation. DIR provides displacement vector field (DVF) which defines the voxel to voxel mapping between the fixed image and the moving image. There are several steps to perform DIR (Klein and Staring 2008). Image metrics measures similarity distance between images. Optimizer aligns the images as good as possible based on the measures. Then the moving image is transformed toward the fixed image based on the optimization result (Fig.10).

Table 5: Example of image coordinates of SIM-CT vs. CBCT

	SIM-CT	CBCT
Origin (mm)	-275, -614, 128.383	-449.414, -449.414, -79.5
Element Spacing (mm)	1.074, 1.074, 3	1.172, 1.172, 3
Dimension Size	512, 512, 75	384, 384, 53

Figure 10: DIR includes similarity measure, optimization, transformation and interpolation.

3.2.3.1 Image Metrics

Either point based or intensity based method is used for similarity measures (Xing L 2007). Point based methods minimize the difference of the points on the surface of anatomical structure. A large amount of landmarks need to be selected to achieve good representation which takes lots of manpower. Intensity based method measures the voxel intensity difference directly which is accurate, fast and less human interaction needed. There are several different similarity measurers available in ITK: sum of square (SSD), mean of square (MS), and mutual information (MI) etc (Luis, et al. 2005).

- Sum of square

SSD is the sum of squared intensity difference. N is number of pixels. F_i is the i^{th} pixel in the fixed image and M_i is the i^{th} pixel in the moving image. SSD is only applicable in single modality registration since it is very sensitive to large intensity difference.

$$SSD = \sum_{i=1}^{N} (F_i - M_i)^2 \quad \textbf{(7)}$$

- Mean of square

MS is the mean squared pixel intensity difference between the fixed image and the moving image.

$$MS = \sum_{i=1}^{N} (F_i - M_i)^2 / N \quad \textbf{(8)}$$

- Mutual Information

MI measures the correlation of image intensity from the fixed image to the moving image. It is computed based on the entropy. The entropy is the very important concept in thermodynamics which describes the disorder in a system. In information theory, the entropy represents the amount of information in one image to reduce the uncertainty in the other image. The entropy in the fixed image is described as

$$S_F = -\int p_F(i) \log_2 p_F(i) di \quad \textbf{(9)}$$

The entropy in the moving image is described as

$$S_M = -\int p_M(j) \log_2 p_M(j) dj \quad \textbf{(10)}$$

The joint entropy of the fixed image and the moving image is described as

$$S_{F,M} = -\int p_{F,M}(i,j) \log_2 p_{F,M}(i,j) didj \quad \textbf{(11)}$$

Where p_M and p_F is the marginal probability density functions of the fixed image and moving image respectively. $p_{F,M}$ is the joint probability density function between the two images. The MI is defined as the difference of the entropy

$$\mathrm{MI} = \mathrm{S_M} + \mathrm{S_F} - \mathrm{S_{F,M}} \quad \textbf{(12)}$$

Combine equation 9-12, MI is calculated by

$$MI(F,M) = \int_F \int_M p(f,m) \log_2 \left(\frac{p(f,m)}{p_F(f) p_M(m)} \right) dfdm \quad \textbf{(13)}$$

MI has become the standard DIR, especially in multi-modality registration (Pluim and Maintz 2003). MI was used to evaluate intensity metrics between SIM-CT and CBCT in my work for DIR.

3.2.3.2 Optimizer

Optimization algorithm has various applications. In the image registration, the optimizer optimizes the transformation parameters to minimize the cost function which is the similarity metrics. There are two types of optimizers in ITK, single valued optimizer and multiple valued optimizer. The single valued optimizer is suitable for the cost function of image registration which returns a single value. Gradient descent (GD) and Robbins-Monro (RM) are both single value optimizers to obtain optimal transformation parameter.

- Gradient descent

The optimization starts at a zero shift position of two image sets. The direction for the next step is set as the negative gradient of the cost function (Fig.11). The next position will be

$$x' = x - h * f'(x) \quad \textbf{(14)}$$

where x is the current position, x' is the next position, h is step size and f(x) is the cost function. The step size is crucial to tune the optimization. If the value is too high, the image may be deformed beyond recognition. If the value is too low, the optimum may not be reached. The local minimum can be avoided with appropriate value of step size.

Figure 11: The optimization starts at the initial position. The direction of the descent is the negative derivative of the cost function. The new position is updated at each iteration based on the step size.

3.2.3.3 Transformation

There are many algorithms to determine the deformation between the fixed and moving images. ITK offers a variety of transforms. Two common ones are Demons and B-Spline.

- Demons

The demons were first introduced by Maxwell in the 19th century to illustrate thermodynamics. Two different types of particles were separated by the membrane in a container. The demons existed in the membrane which allowed one type of particles to diffuse over but not the other type of particles. Thirion's demons algorithm applies similar concept by diffusing the deformed image through the contour of the objects in the fixed image through demons (Thirion 1998). The boundaries in the fixed image are considered as membrane. The deformed grid which represents the deformed image diffuses through the

interfaces. The deformed grid can be rigid or allow for more freedom depending on types of deformation. The force, derived from gradient information of the fixed image, deforms the moving image based on the intensity difference between the two image sets. At each voxel level, the force pushes the voxel in the moving image toward the fixed image. The deformation field is defined as

$$\vec{u} = \frac{(m-f)\vec{\nabla} f}{\left|\vec{\nabla} f\right|^2 + (m-f)^2} \quad \textbf{(15)}$$

Where m and f are the external forces of the fixed and moving image respectively, $\vec{\nabla} f$ is the gradient of the surrounding force.

- B-Spline

B-Spline transformation generates deformation vector of every control point defined on a coarse grid which is the B-Spline grid. The B-Spline grid can be defined differently in each direction based on the dimension of the 3D image. The DVF is computed using B-Spline interpolation based on the existing deformation values on the grid. It is a local deformation method which means the transformation of a point can be computed from the surrounding points only. To compensate for the limitation, a rigid or affine transformation needs to be performed first. The deformation field is defined as

$$M_k(x) = x + \sum_i \sum_j \sum_k p_{i,j,k}(x - x_i)(x - x_j)(x - x_k) \quad \textbf{(16)}$$

3.2.3.4 Interpolator

During the optimization, the intensity value is compared in the fixed image against the corresponding value in the deformed image. Since the fixed image has different grid size compared to the moving image usually, the grid points are mapped to non-rigid positions in general. Interpolator is necessary to evaluate

the intensity value of these non-grid points on the moving image. There are several ways to do interpolation - linear interpolation or N^{th} order B-Spline. The higher order of the B-Spline function, the better quality is achieved but with more computation time. When N is one, B-Spline becomes linear interpolation.

3.2.3.5 Multi-resolution

It is not necessary to select all voxels in the fixed image to calculate MI since it costs a lot of memory and time to calculate huge amounts of data. The multi-resolution approach can improve the registration speed, accuracy and robustness. A grid which down samples the fixed image is defined for each resolution level to generate MI. The sampling starts at a coarse level and is tuned at the next finer scale. The process can be repeated at multiple levels until it reaches the finest scale possible. The multi-resolution strategy can reduce data and transformation complexity to get better and more flexible DIR (Lester and Arridge 1999).

3.2.4 Evaluation on DIR

The difficult problem of DIR is to evaluate whether the registration is successful. The rigid registration is easy to verify based on the structures or some landmarks since all the voxels are shifted together toward the same direction. However, it is impossible to track where each voxel is mapped to visually. The evaluation of the DIR can be done quantitatively or qualitatively, such as checking the fiducial markers, comparing images side by side, and validating the registration with voxel level based algorithm.

- Fiducial markers based validation

Three Acculoc gold seed fiducial markers (Northwest Medical Physics Equipment, MEDTEC Company, Orange City, Iowa) are implanted in the prostate gland of patients enrolled in the IGRT protocol. The primary objective of the protocol is to compare the range of agreement of patient shifts given by each image modality, U/S. vs. in-room orthogonal KV images using fiducial markers vs. CBCT. One seed should be placed in the base of prostate on the left or right side. The second one should be placed toward the mid-prostate gland. The third one should be implanted toward the apex. The dimension of the markers is about 1mm in diameter and 3mm in length. These seeds could be tracked to evaluate the accuracy of the registration. However, the drawback is that three markers are insufficient to validate the registration accuracy of the entire volume.

- Image comparison side by side visually

The deformed image should be exactly same as the fixed image ideally. The two images can be overlaid on top of each other and checked by split view, chess view, blending view or spy glass. However, CBCT has relative poor quality due to larger scatter contribution. In prostate scan, the boundary between prostate and rectum is blurred and difficult to evaluate. Such comparison is also subjective based on the reviewer.

- Unbalanced energy (UE)

The DVF accuracy is vital to achieve accurate dose reconstruction of deformed organ. For the low intensity region like prostate, the displacement variations are relatively insensitive to the similarity metrics which may result in DIR error. The poor image quality in the prostate region of CBCT also makes the

validation of registration difficult. Zhong proposed an automatic method using UE to quantify the DVF error (Zhong, Peters and Siebers 2007).

The method characterizes the organ deformation similar to the displacement and elastic force used in the solid continuum mechanics. The organ is simulated as an elastic body without any external forces acting inferiorly. At the equilibrium position, the work done by the external forces on the organ surface will be equal to the energy from the tissue deformation while internal forces at each node must be zero. The elastic force at each node contributing from the neighboring elements is defined as

$$F_i = K_{ij}^e \times d_j = E^e m_{ij}^e d_j \quad \textbf{(17)}$$

where K^e is the stiffness matrix of the elastic material, E^e is Young's modulus of the element e, d_j is the displacement factor of j^{th} vertex and F_i is the external force to the node i. The unbalanced force at each vertex j is defined as

$$\tilde{F}_i = \delta \tilde{f}_i^{(D)} + \delta \tilde{f}_i^{(E)} \quad \textbf{(18)}$$

The unbalanced force is due to two sources. One is inaccurate material E_0 which is the assigned initial Young's modulus and the other is an unknown displacement factor approximated by DVF. The UE is the product of the unbalanced force and the DVF. UE can be used to assess the registration performance based on its value. The lesser the value is, the better DIR is performed on the vertex. By assigning the value to the vertices of each element, the 3D UE images can be reconstructed to evaluate the DIR.

3.2.5 Dose Reconstruction and accumulation

The dose for each treatment fraction is recalculated on CBCT with exactly same treatment plan parameters (beam angle, MU, fluence and calculation algorithm etc.). The dose grid size is set to 0.25cm. Since the dose grid is not the same as the B-Spline grid, DVF cannot be applied to the dose grid directly. The CBCT dose is first warped back to the SIM-CT image grid with the direct approximation using the transformation matrix. The closest neighboring points on the SIM-CT image grid are estimated by the B-Spline interpolation. Then the warped dose on the SIM-CT is resampled to match the location on the planning dose grid with B-Spline interpolation method. Fig.12 shows the two steps for the dose reconstructions.

Since all fraction doses warped from SIM-CT have the same grid size of the planning dose, the dose accumulation is performed by adding the dose value of each point on the dose grid. If the CBCT is not acquired during the treatment due to the OBI problem, single fraction planning dose is used to represent dose for the treatment session.

Figure 12: Dose reconstruction. (a) dose was recalculated on the CBCT after rigid registered with SIM-CT, (b) warp dose by applying the transformation matrix generated in DIR, (c) resample the warped dose from B-Spline grid to the dose grid.

3.2.6 The Flow of ART

The ART can be described as a closed-loop control (Zerda, B and Xing 2007). The conventional treatment planning 3D or IMRT is open-loop control. There is no feedback of the ongoing treatment to update patient's anatomy information. For the closed-loop control, the treatment planning can be repeated as a loop with the feedback of CBCT to represent the updated patient geometry. The framework for ART is shown in Fig.13. The patient was treated with IMRT plan based on the SIM-CT. CBCT was acquired before each treatment for online setup. The patient was shifted based on the rigid registration result of CBCT and SIM-CT. Dose was recalculated on each CBCT with the same plan. The DIR was performed and evaluated offline and the DVF was generated accordingly. Dose

was reconstructed and accumulated to reflect the actual dose delivered to the patient. Then the adaptive plans at any fractions were compared to the original plan to evaluate the deviation of PTV coverage and OAR dose limit. If the actual dose delivered to PTV deviated clinically significant from the prescription dose for the given fractions, or if OAR received higher dose than expected, the treatment plan would be re-optimized based on the previously delivered dose. The criteria to trigger re-optimization were clinical assessments. My study focused on the treatment planning outcome to come up with the feasible optimization schedule to achieve the balance of PTV dose coverage and inhomogeneity, OAR dose constraint and time involved.

Figure 13: The flow chart of ART. The patients are treated with IGRT protocol. DIR and dose reconstruction are performed offline. The plan is evaluated and optimization necessity is considered.

With the ART applications, the systematic error for the prostate treatment should be reduced; therefore the smaller margin should be enough to account for all the setup errors, prostate motion and random errors. If it is valid, the ART not only compensates for dose deficiency due to organ deformation but also has significant benefits of reducing organ toxicity, which makes planning easier and PTV coverage more homogeneous and allow for further dose escalation. The study addressed such potential benefit of ART. For each patient, two new IMRT plans were produced using the SIM-CT with a smaller margin applied to the CTV. The PTV margin for the original plan was 10mm around and 6mm posterior. The margin was reduced to 5mm around except 3mm posterior for one IMRT plan and 3mm all around for the other plan. The new plans were applied to each CBCT set and the adaptive procedures were repeated to generate actual dose delivered. The 5/3 mm margin was selected since it had been used by multiple clinical trials. The prostate intra-fraction motion was around 2-3mm based on the results of Calypso® protocol at Henry Ford Hospital (Fig.14). Considering all other uncertainties, such as image resolution, DIR registration accuracy, and dose reconstruction, 3 mm was at the lower end of the margin's confidence level to account for the motion of the target.

Figure 14: Three calypso beacons were implanted toward the apex, the left base and the right base of the prostate gland. These beacons provided real time tracking during the treatment delivery. The detected radiation was shown as shaded area on the report. If the offset was larger than 5mm in one or more axes, the treatment was stopped immediately. The prostate motion was very stable for most treatments where the offset was less than 2mm usually.

3.2.7 Plan evaluation – Radiobiological Model

The treatment plan is evaluated routinely by utilizing the dose-volume histogram (DVH). DVH indicates the amount of volume of interest that receives a certain dose or higher. The dose value can be re-sampled into equi-spaced intervals. Then the volume of the voxels receiving dose within the interval is accumulated. The cumulative DVH is obtained by adding the voxels receiving a specified dose or more. However, even though DVH shows dose coverage of a volume, it does not contain any spatial information of the dose distribution. Cold spots in a small volume of tumor may not have noticeable impact on the DVH but

the tumor control can be diminished as a result. Therefore DVH can be a good supplement to isodose distribution in the plan evaluation, but not as a sole standard. Radiobiological model has been used to evaluate and predict the clinical outcome in terms of both a tumor control probability (TCP) and normal tissue complication probability (NTCP). The treatment plan can be ranked using the biological data, volumetric dose distribution and the DVH for different organs.

3.2.7.1 TCP

TCP describes the probability of killing tumor clonogenic cells in the TV for a given dose. All TCP models have similar assumption that the lesion is killed if all clonogenic cells are destroyed by radiation. The TCP in the study is poisson statistics-based model. The model assumes that dose response for tumor is sigmoidal in shape and the number of surviving clonogens follows poisson distribution coupled with Linear-Quadratic (LQ) model. The model is express as

$$TCP = e^{-\sum_i N_i SF_i(D_i)} \quad \textbf{(19)}$$

Where N_i is the initial clonogenic cells density of the voxel i in the tumor, $SF_i(D_i)$ is the surviving fraction of the voxel i at given prescription dose. The assumption is made that the clonogenic cells are evenly distributed across PTV. The common expression of surviving fraction calculated by the LQ model is

$$\boldsymbol{SF = e^{-(\alpha D - \beta D^2)}} \quad \textbf{(20)}$$

Where α represents the probability of double chromosome break which is irreparable and β represents the probability of single chromosome break which is reparable. If the fraction dose is not 2Gy, SF can be calculated biologically equivalent from SF_2,

$$SF = SF_2^{D/2} \quad \textbf{(21)}$$

Where SF_2 is the surviving fraction at 2Gy and D is the prescription dose.

In order to get tumor control data, patients need to have adequate follow-up. There are different estimations of prostate TCP parameters (Webb 1994) (Webb and Nahum 1993) (Sanchez-Nieto and Nahum 1999). The TCP model shows that SF_2 and N_0 are the dominant factors of radio-resistance in prostate cancer. SF_2 ranges from 0.5 to 0.6 and N_0 is about $10^4 – 10^7$ cells/cm^3. The α/β ratio tells the sensitivity of the tissue response to fractionation effects. Tumor α/β value is usually 10Gy since they are accutely responding tissues. Late effect usually occurs in slowly proliferating tissue such as bladder or rectum which has α/β ratios of 2.5-5 Gy and 3-7Gy respectively. However, it is now believed that the α/β value is much lower for prostate tumors. α/β value of prostate is estimated ranging from 1-5 Gy from a large multicenter database, such as the university of Michigan, Royal Brisbane Hospital, and the William Beaumont Hospital (Brenner, 2002) (Folwer and Ritter 2001)). Fowler et al. estimated α/β ratio for prostate cancer is about 1.5Gy which may be even lower than the surrounding late responding normal tissue (Fowler and Ritter 2003).

3.2.7.2 NTCP

NTCP model describes the probability of unfavorable reactions in normal tissue responding to radiation. Four parameter LKB-NTCP model was fit to normal tissue tolerance data (Emami, et al. 1991) (Burman, Kutcher and Emami 1991). The model assesses the possibility that complication will occur for a given dose no matter how small the partial volume is. The model is described as

$$NTCP = \frac{1}{\sqrt{2\pi}} \int_{-\infty}^{t} e^{-t^2/2} dt \quad \textbf{(22)}$$

$$t = \frac{D - TD_{50}(\upsilon)}{m \cdot TD_{50}(\upsilon)} \quad \textbf{(23)}$$

$$\upsilon = \boldsymbol{V/V_{ref}} \quad \textbf{(24)}$$

$$EUD = (\sum_{i=1}^{N} D_i^{1/n} \frac{V_i}{V_{tot}})^n \quad \textbf{(25)}$$

Where TD_{50} is defined as dose received by the volume that could lead to a complication probability of 50 percent, V_{ref} is the volume for TD_{50}, m is the slope of the complication probability vs. dose curve, and n is the volume dependence of the complication probability. n differs the tolerance dose for partial and whole organ. When n is close to zero, the volume effect is small and when n is close to 1, the volume effect is large. The organ with a smaller n indicates a serial organ and the one with a large n can be qualified as a parallel organ. If any portion of a serial organ receives the dose above the tolerance, it loses the complete functionality. If a large volume of a parallel organ receives the dose above the tolerance limit, it is considered damaged.

The model parameters are generated by curve fitting. Patients are followed up to evaluate genito-urinary (GU) and gastro-intestinal (GI) complication. The side effect of GI is diarrhea, rectal pain, rectal bleeding, rectal ulceration, and rectal fistula. The side effect of GU is incontinence, persistent urinary retention, increased urinary frequency/urgency, and urethral stricture. Emami et al (Emami and Lyman, 1991) provided tolerance dose for whole organ irradiation listed in table 6. However the data for volume dependence was not

sufficient. The tolerance data was only for one volume. There could be more uncertainty and less confidence for the fitted parameters.

Table 6: NTCP parameters published by Emami

Organ	V_{ref}	TD_{50}	n	m	End Point
Rectum	Whole Organ	80	0.12	0.15	Severe necrosis/fistula/stenosis/proctitis
Bladder	Whole Organ	80	0.5	0.11	Symptomatic bladder contracture/Volume loss

The quality and quantity of clinical data have begun to improve significantly in the last decade. Several other groups provided estimated parameters for the LKB model by fitting to the late GU/GI toxicity data. The GU parameters shown in table 7 were generated from 128 patients with prescription dose 78 Gy (Cheung, Tucker and Lei 2007). n was very close to zero which means the toxicity was directly related to the maximum dose to bladder. The Italian multi-centric study fitted the late rectal bleeding data using the NTCP model listed in table 7 (Rancati, Fiorino and Gagliardi 2004). It showed that the models fitted the complication very well in qualitative and quantitative comparisons. It also suggested that the rectum is a serial organ.

Table 7: NTCP model parameters fitted to the late GU/GI toxicity from other research groups

Organ	**TD_{50}**	**n**	**m**	**End Point**
Rectum	81.9	0.23	0.19	Grade2/3 late bleeding
Rectum	78.6	0.06	0.06	Grade 3 late bleeding
Bladder	77.6	0.00995	0.022	Grade >=1 late GU toxicity

3.2.8 Re-Optimization

The optimization must make a balance between sufficient tumor coverage and sparing OAR. There are generally two categories in the optimization algorithms: deterministic methods and stochastic methods. The deterministic methods include gradient descent and maximum likelihood. The stochastic methods include simulated annealing and genetic algorithms. The optimization uses objectives functions in terms of dose-volume. The upper objective is used to limit the hotspot in the target and the dose in other OAR. The lower objective is used to define the dose level in the target to receive at least a specified dose for a certain percentage of volume. The objective function can be written in a weighted least square model

$$\boldsymbol{OF = w_k \sum_{i=1}^{N} (D_k^i(x) - D_k^{obj})^2} \qquad \textbf{(26)}$$

Where w_k is the weight for organ k, D_k^i is the dose at voxel i in organ k and D_k^{obj} is the objective dose constraint to the organ. The cross section of a beam is broken into beamlets of the equal dimensions. Intensity is constant within each individual beamlet. But different beamlet may have different intensity. The optimization process minimizes the weighted sum of discrepancy from target prescription dose and OAR constraint dose by adjusting the intensity level of each beamlet. The final fluence maps are generated when the desired dose distribution is achieved. The smoothing function is applied in both directions of the fluence before leaf motion calculations to improve deliverability of the fluence and minimize the beam-on time. The leaf sequencing is calculated to convert the fluence map into deliverable MLC leaf motion, taking MLC limitations and design

into consideration. The leaf motion can be calculated for segmented or dynamic delivery. The segmented MLC motion sequence has multiple static apertures. The beam is turned on when the leaves stop and is turned off when the leaves move to the next segment. The leaves move continuously with variable speeds while the beam is on with a variable dose rate, for the dynamic MLC sequence delivery.

Figure 15: A. At least 99% of PTV receives at least 8000cGy. B. The maximum dose received by PTV should be less than 8200cGy. C. No more than 10% of the rectum receives more than 7000cGy.

The initial guess accumulated dose of the previously treated sessions is used as a baseline for the new optimization and the objective function is minimized for the remaining fractions. The new optimal fluence map is generated

and dose is recalculated for the remaining sessions to assure that the composited dose deposition satisfies the original prescription.

3.3 Results & Discussion

3.3.1 HU-ED Calibration for CBCT

The average HU number was plotted against the known relative electron density for both SIM-CT and CBCT (Fig.16). Error bars showed the standard deviation of HU numbers of the measurements. The two curves were well correlated. Also the HU number calibration accuracy depended on the phantom insert material. The larger discrepancy was shown in the high density region. The high density insert made of Teflon has been reported as a less than ideal tissue substitute (Craig, Brochu and Vandyk 1999). In the human bony structures, HU would be higher for the same electron density due to higher atomic numbers of calcium. The non-linear correction was carefully examined regarding the effect of HU difference on dose calculation using CBCT.

3.3.2 Dose calculation on CBCT

3.3.2.1 Four-field box calculation with and without inhomogeneity correction

The traditional 3D plan of four opposed fields using 6MV beam was calculated on the rando phantom image with and without inhomogeneity correction. If the inhomogeneity correction was turned off, the D_{mean} between SIM-CT and CBCT was only 0.1% different and D_{max} was 0.3% different in the target. The difference of D_{min} was 1.2%. The isodose distribution and DVH comparison between the two images sets were compared in Fig. 18.

Figure 16: HU and relative electron density for SIM-CT vs. CBCT.

When the inhomogeneity correction was on, the minimum dose showed up to 5% difference for the prostate and OAR. However, the mean doses agreed very well between SIM-CT and CBCT. Table 8 shows dose statistics comparison of the two plans. The isodose distribution and DVH were displayed in Fig.18. The dose distribution deviated slightly between CBCT and SIM-CT. However, the similarity between the two plans was well within the clinical tolerance.

(a)

(b)

(c)

Figure 17: 3D plan without inhomogeneity correction. (a) Isodose distribution in the SIM-CT. (b) Isodose distribution in the CBCT. (c) DVH comparison of prostate (red), rectum (brown), and bladder (blue) between SIM-CT (square) and CBCT (triangle).

(a) (b)

(c)

Figure 18: 3D plan with inhomogeneity correction. (a) Isodose distribution in the SIM-CT. (b) Isodose distribution in the CBCT. (c) DVH comparison of prostate (red), rectum (brown), and bladder (blue) between SIM-CT (square) and CBCT (triangle).

Table 8: Minimum dose, maximum dose and mean dose for prostate, rectum and bladder using four-field box technique with inhomogeneity correction

	Prostate			*Rectum*			*Bladder*		
	D_{min}	D_{max}	D_{mean}	D_{min}	D_{max}	D_{mean}	D_{min}	D_{max}	D_{mean}
SIM-CT	89.1%	103.1%	99.2%	26.3%	102.1%	61.9%	40.5%	100.5%	59.3%
CBCT	94.1%	103.4%	99.5%	31.8%	102.6%	61.9%	43.7%	100%	59.1%

3.3.2.2 IMRT Dose Calculation

The 9 uniformly spaced fields IMRT plan that is routinely used for prostate treatment was applied to the rando phantom for comparison between calculations based on SIM-CT and CBCT. The plan was optimized and calculated on SIM-CT. And the plan with same fluence and MU was recalculated on a co-registered CBCT image. The comparison between the two plans is summarized in table 9 and Fig19. CBCT plan showed slightly more inhomogeneous dose distribution with 1% higher maximum dose and 5% higher minimum dose. The prescription isodose coverage on target correlated well between SIM-CT and CBCT. Rectum maximum dose calculated on CBCT image was 1.6% less than that calculated on SIM-CT. Bladder dose showed more discrepancy. The maximum dose had about 17% difference and mean dose had about 1% difference.

Table 9: Minimum dose, maximum dose and mean dose for prostate, rectum and bladder using 9 fields IMRT

	Prostate			*Rectum*			*Bladder*		
	D_{min}	D_{max}	D_{mean}	D_{min}	D_{max}	D_{mean}	D_{min}	D_{max}	D_{mean}
SIM-CT	70.2%	102.7%	99.2%	3.3%	97.6%	18.3%	4.3%	99.3%	18.4%
CBCT	75.2%	103.6%	99.6%	3.4%	96.0%	18.2%	4.5%	82.6%	17.1%

(a)

(b)

(c)

Figure 19: 9 fields IMRT plan. (a) Isodose distribution in the SIM-CT. (b) Isodose distribution in the CBCT. (c) DVH comparison of prostate (red), rectum (brown), and bladder (blue) between SIM-CT (triangle) and CBCT (square).

3.3.3 DIR and Validation

3.3.3.1 DIR and Validation on Computer Generalized Pelvis Phantom

The parameters for the DIR were tuned and the results were evaluated based on the computer generated pelvis phantom (Fig.20). The phantom image grid had 160x160x160 voxels with voxel size 1mm in all three dimensions. There were geometrical shapes in the image that represent bladder, rectum, prostate and femoral heads. The deformable phantom images were derived based on the DVF created from DIR on a patient (Zhong, Kim and Chetty).

(a) (b)

Figure 20: The pelvis phantom used for the evaluation of DIR. (a) the fixed image, (b) the moving image which is derived from known DVF

The parameters to achieve the phantom result are listed in table 10 and were applied to DIR between SIM-CT and CBCT for all patient treatment sessions. The deformed image was generated [Fig.21(a)] and compared to the fixed image [Fig.21(b)]. The image registration error was difficult to detect by visual comparison in such case. Since DVF was already known to reconstruct the

deformed image, DIR result could be quantitatively evaluated voxel by voxel, by comparing DVF created from B-Spline registration and the known DVF.

Table 10: B-Spine registration tuned parameters

Image Resolution Levels	4	
Mutual Information	Number of spatial samples at each level	4096, 4096, 8192, 16384
	Number of grey levels	16, 32, 64, 64
B-Spline Interpolator	Each resolution level	1, 1, 1, 1
	Final Deformation	3
Optimization	Maximum number of iterations at each level	8000, 8000, 8000, 8000
Transformation	B-Spline Grid Spacing	10x10x5 voxels

(a) (b)

Figure 21: B Spline DIR on pelvis phantom. (a) the deformed image from the moving image, (b) the fixed image

Fig. 22 demonstrated the B-Spline registration accuracy. The agreement was within sub millimeter for all voxels along the central line from anterior to posterior. A larger discrepancy (over 1mm) was observed at the anterior boundary region. It showed that the error was increased in the large deformation region at the boundary for the B-Spline registration.

Figure 22: DVF Displacement of benchmark and B-Spline of each voxel in AP direction.

3.3.3.2 DIR and Validation on Prostate Patients

Deformable registrations were performed between CBCT and SIM-CT for all fractions of five patients. The registration errors were detected by three methods for a comprehensive evaluation. Since all the patients were implanted with three fiducial markers, the relative positions of the markers between the SIM-CT and the deformed CBCT were calculated to evaluate the registration error. The registration error in the rigid registration was also calculated for comparison.

Figure 23: The displacement of the three seeds for each fraction after DIR and rigid registration. (a) seed 1 offset between SIM-CT and deformed CBCT in Rt Lat-Lt Lat, Anterior-Posterior, Superior-Inferior direction, (b) seed 1 offset for the rigid registration in all three directions, (c) seed 2 offset between SIM-CT and deformed CBCT, (d) seed 2 offset for the rigid registration, (e) seed 3 offset between SIM-CT and deformed CBCT, (f) seed 3 offset for the rigid registration. Blue bar is L-R direction. Red bar is A-P direction. Yellow bar is S-I direction.

The offset of the seed was calculated by calculating the difference of voxel index at the center of the seed between the fixed image and the deformed image. The voxel dimension in z direction was 3mm, which was the slice thickness of CT scan. It was larger than the voxel size of 1.07mm in x and y planes. Therefore, the displacement was larger in superior-inferior direction, even though the voxel index offset was similar, compared to the other two directions. The comparison of

the seed position accuracy between DIR and rigid registration is shown in Fig. 23. The bar showed the offset in mm comparing the seed position of the SIM-CT and registered CBCT for each fraction. The offset measurement was skipped if the CBCT was not performed at the beginning ot the treatment session due to some technical problems. The seed positions correlated very well between SIM-CT and deformed CBCT after DIR. The DIR results demonstrated that this method was more accurate than the rigid registration. The mean and standard deviation were calculated for each seed in three dimensions after the rigid registration and DIR and are shown in table 11. The mean and standard deviation in left-right direction was 0 mm and 1 mm correspondingly. But the mean was 2-4mm in the ant-post and sup-inf directions and the standard deviation was about 2 mm. After DIR, the mean in all three directions became 0 and the standard deviation was less than one millimeter.

Table 11: Statistics of seeds offsets in all three dimensions after rigid registration and DIR

		X (mm)	Y (mm)	Z (mm)
Rigid	Seed1	0±1.16	3±2.06	3±2.48
	Seed2	0±1.21	3±1.87	4±2.6
	Seed3	0±1.50	-2±2.14	4±2.47
DIR	Seed1	0±0.40	0±0.47	0±0
	Seed2	0±0.51	0±0.54	0±0.5
	Seed3	0±0.50	0±0.52	0±0.50

Evaluation of seed positions could provide quantitative analysis of the accuracy of DIR. However, three seeds could not represent the entire target volume information. It was not a valid strategy to validate DIR by relying on seeds only. Visual comparison of SIM-CT and deformed CBCT slice by slice was a good supplemental method to validate the registration qualitatively. But it was time consuming and a subjective method. Also it was difficult to detect errors in a millimeter range with a naked eye. However, the UE was able to detect the registration error automatically and quantitatively in 3D. The UE value was derived by the assigned DVF on the vertices of image grid in three directions. The UE image was reconstructed for the sampling voxels and the value was taken by averaging the number in three directions. The darker region represented lower UE and the brighter region showed higher UE. The lower the value of UE was, the higher the quality of DIR was achieved. To reduce the calculation time and to focus on the ROI, the UE image was cropped to the prostate and OARs nearby. The corresponding SIM-CT images, deformed CBCT images and UE images were sampled in Fig.24 for validation of DIR. There was a brighter region in the UE image shown in the first row, which indicated higher UE. It was also observed that there was a distortion in the seminal vesicles in the deformed CBCT image compared to the SIM-CT image. The UE value was pretty low in the prostate region, which indicated good performance of the image fusion. UE calculated by a finite element based framework could be a very effective tool to evaluate DIR in clinical settings. DIR between SIM-CT and CBCT for all fractions were validated by three different ways for a comprehensive

evaluation. The generated transformation matrix was used for the dose reconstruction.

(a) (b) (c)

Figure 24: DIR validation. (a) SIM-CT images with every 9mm spacing, (b) corresponding deformed CBCT images (c) the cropped UE images in the ROI.

3.3.3.3 Dose Reconstruction

The dose calculated on CBCT could be warped by applying transformation matrix. The transformation matrix was based on the B-Spline grid in DIR. The reconstructed dose would have same dimension of image grid. In order to accumulate the dose and compare with the planned dose, the warped dose was resampled using B-Spline interpolation to match dose grid size calculated in SIM-CT. One example was shown in Fig.25. Fig.25 (a) showed one dose plane calculated in CBCT. The dose matrix size was 159x111x53. The warped dose in Fig.25 (b) had dimension 512x512x75 which was same as SIM-CT image size. It was resampled to the dose grid size calculated for SIM-CT which was 159x110x75.

Figure 25: Dose reconstruction. (a) dose calculated on CBCT (b) warped dose by applying transformation matrix (c) resampled dose to match dose grid size in SIM-CT.

After the doses calculated for each treatment session were warped and resampled, they can be directly added up since all of them had same grid size (Fig.26). If CBCT was not acquired for a certain fraction, the single fraction planned dose was used as a substite. The accumulated doses at any treatment session were calculated and compared to the planning dose to assess the ongoing treatment dose deposition. Re-optimization could be scheduled if the

target coverage was not achieved by a specified fraction or an OAR has received the dose over the tolerance limit.

Figure 26: Warped dose for each treatment session was accumulated to generate total delivered dose at any fraction.

3.3.4 Target Evaluation

The isodose distributions between a treatment plan (plan) and a real delivery (real) were compared slice by slice in three different views for each patient. Fig.27 represented the comparison between a planned dose and a delivered dose for the patient #4. The isodose distributions in the two cases were very close to each other in all three margin settings. The CTV was well covered by the prescription dose in all cases. The maximum and minimum doses were different slightly in the CTV. Rectum and bladder doses varied a lot in each case.

Figure 27: Isodose comparison between "plan" and "real". (a) plan dose distribution with PTV margin 10/6 mm, (b) real dose distribution to plan with PTV margin 10/6 mm, (c) plan dose distribution with PTV margin 5/3 mm, (d) real dose distribution to plan with PTV margin 5/3 mm, (e) plan dose distribution with PTV margin 3 mm, (f) real dose distribution to plan with PTV margin 3 mm.

Mean, minimum and maximum doses to CTV for each patient are summarized in table 12. With 10 mm margin, planned dose statistics for the CTV were very close to the real one for all five patients. Differences of mean, minimum and maximum doses of CTV were all within 2%. When the margin was reduced to 5/3 (everywhere/posterior) mm, CTV minimum dose showed larger discrepancy and the difference was about 5% for three patients and 1% for the other two. CTV mean and maximum doses were in agreement within 2%. When the margin moved to 3mm, the difference of CTV minimum dose was 4-7% while mean and maximum doses were still within 2%. As the margin was reduced, a

tiny portion of CTV could be underdosed since it might move out of the treatment fields in some fractions. However, it did not have a big clinical impact because underdosed region was very small. Sometimes there were just several voxels that were moved outside of the prescription isodose line. For all five patients, real mean doses to CTV were all within 98% of planned mean dose in 3 mm margin setup.

Table 12: Dose statistics comparison of CTV between planned dose and real dose at three different margin settings

Patient		Plan Dose 10/6	Real Dose 10/6	%Diff	Plan dose 5/3	Real Dose 5/3	%Diff	Plan Dose 3	Real Dose 3	%Diff
1	Min Dose	7656	7749	1.2%	7583	7508	-1.0%	7435	7131	-4.1%
	Mean Dose	7871	7891	0.3%	7872	7871	0.0%	7933	7837	-1.2%
	Max Dose	8234	8283	0.6%	8290	8231	-0.7%	8252	8135	-1.4%
2	Min Dose	7903	7997	1.2%	7990	7617	-4.7%	7733	7193	-7.0%
	Mean Dose	8357	8277	-1.0%	8465	8367	-1.2%	8497	8362	-1.6%
	Max Dose	8766	8625	-1.6%	8886	8745	-1.6%	8895	8746	-1.7%
3	Min Dose	7629	7622	-0.1%	7613	7240	-4.9%	7601	7276	-4.3%
	Mean Dose	7761	7761	0.0%	7784	7783	0.0%	7809	7791	-0.2%
	Max Dose	7933	7932	0.0%	7964	7932	-0.4%	7961	7930	-0.4%
4	Min Dose	8083	8018	-0.8%	8033	7935	-1.2%	8100	7800	-3.7%
	Mean Dose	8205	8103	-1.2%	8239	8131	-1.3%	8246	8130	-1.4%
	Max Dose	8359	8229	-1.6%	8417	8297	-1.4%	8417	8284	-1.6%
5	Min Dose	7589	7690	1.3%	7257	7629	5.1%	7227	7529	4.2%
	Mean Dose	7852	7808	-0.6%	7853	7794	-0.8%	7858	7796	-0.8%
	Max Dose	8102	7974	-1.6%	8130	7967	-2.0%	8136	8013	-1.5%

PTV dose showed much larger discrepancy between the planned dose and the real dose. Generally, PTV dose coverage offset increased more as the margin became smaller. Smaller margin could significantly reduce dose to OARs. But this is accompanied by a higher risk to miss the target. Many factors could account for inter-fraction motion. It was difficult to give a universal margin which

was suitable for all patients. DVH comparisons for each patient are presented in Fig. 28-32. PTV (pink), CTV (red), rectum (brown) and bladder (blue) were plotted to compare planned and real doses. The upper left figure shows the plan with 10 mm margin. The upper right figure shows the plan with 5/3 mm margin. The lower figure is 3 mm margin. The data for the five patients showed that the patient preparation was an important factor in controlling the inter-fraction motion. All five patients were instructed on the bowel preparation, and how to maintain their rectum and bladder filling for each treatment. The patients were scanned with CBCT and corrected for the setup offset for each fraction. If the organs showed larger deformation, patient were taken off the table and instructed to correct the situation by visiting a bathroom and drinking more water afterwards to maintain the bladder filling. However, the results showed that the real PTV dose matched planned dose within 1% for each margin setting for patients 1 and 5. Patient 2 showed a highest discrepancy with the PTV dose coverage. The volume covered by prescription line was 8% less with 5 mm margin and 11% less with 3 mm margin. That patient had more difficulty following the instructions; therefore there was more tissue deformation which could not be corrected by the rigid transformation.

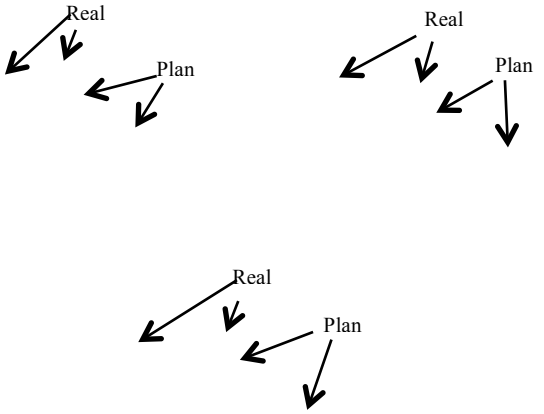

Figure 28: DVH comparison for the three different PTV margins between the treatment plan and the real plan of the patient 1. PTV is the pink line; CTV is the red line; Rectum is the brown line; Bladder is the blue line. (a) With the PTV margin of 10/6 mm; (b) With the PTV margin of 5/3 mm; (c) With the PTV margin of 3mm.

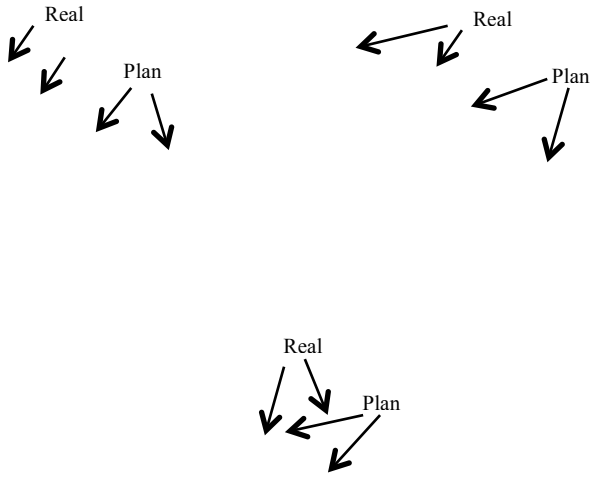

Figure 29: DVH comparison for the three different PTV margins between the treatment plan and the real plan for the patient 2. PTV is the pink line; CTV is the red line; Rectum is the brown line; Bladder is the blue line. (a) With the PTV margin of 10/6 mm; (b) With the PTV margin of 5/3 mm; (c) With the PTV margin of 3mm.

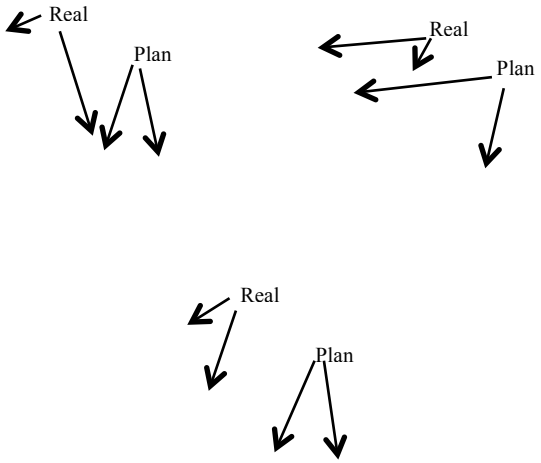

Figure 30: DVH comparison for the three different PTV margins between the treatment plan and the real plan for the patient 3. PTV is the pink line; CTV is the red line; Rectum is the brown line; Bladder is the blue line. (a) With the PTV margin of 10/6 mm; (b) With the PTV margin of 5/3 mm; (c) With the PTV margin of 3mm.

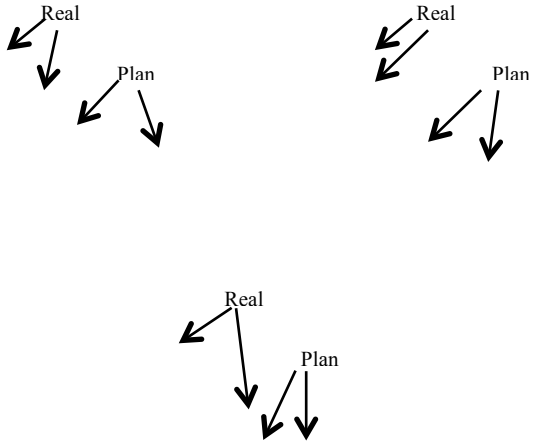

Figure 31: DVH comparison for the three different PTV margins between the treatment plan and the real plan of patient 4. PTV is the pink line; CTV is the red line; Rectum is the brown line; Bladder is the blue line. (a) With the PTV margin of 10/6 mm; (b) With the PTV margin of 5/3 mm; (c) With the PTV margin of 3mm.

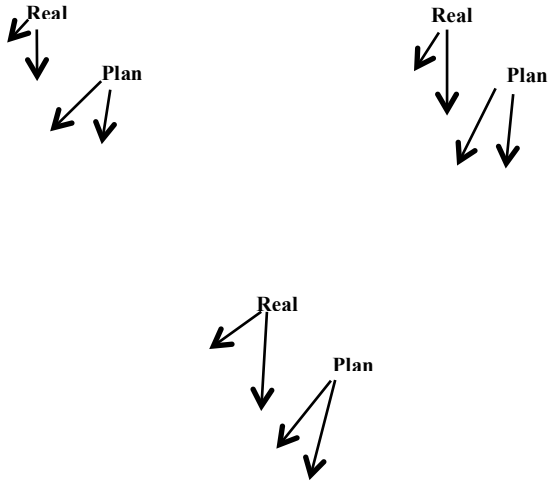

Figure 32: DVH comparison for the three different PTV margins between the treatment plan and the real plan for the patient 5. PTV is the pink line; CTV is the red line; Rectum is the brown line; Bladder is the blue line. (a) With the PTV margin of 10/6 mm; (b) With the PTV margin of 5/3 mm; (c) With the PTV margin of 3mm.

TCP for CTV was also calculated to evaluate tumor control in different margin settings. PTV was not used for the evaluation since the volume was different for each margin. There were many uncertainties for TCP parameters. A lot of debates have been going on in the literature regarding α/β value for prostate, surviving fraction and clonogenic cells density. To avoid any bias, a broad range of numbers was used for TCP evaluation. α/β ratio was varied from 1.5 to 9.5 with an increment of 1. SF_2 values were 0.5 and 0.6, the most probable surviving fraction of tumor cells at 2Gy. The cell density was 10^N /cm^3 where N ranged from 3 to 6.

Figure 33: TCP value vs. α/β ratio of the plan and the real dose delivery for the three margins for the patient 1. N_0 =10,000/cm^3. (a) SF_2 is 0.5. TCP is 1 for each α/β value in all plans; (b) SF_2 is 0.6. TCP difference is within 1% across the range of α/β ratio in each plan. Solid lines connecting the data points are used for the visibility only.

Since the prescription dose to all five patients was either 1.8Gy or 2Gy, there was no hypofraction radiation in the study. The effect of α/β ratio to TCP was minimal. TCP was 100% across α/β region from 1.5 to 9.5 if SF_2 was 0.5 and N_0 was 10^4 (Fig.33 (a)). And the difference was only 1% if SF_2 was 0.6 (Fig.33 (b)). α/β ratio of 4.5, which was the average TCP value across the range, was used for all subsequent calculations.

When SF_2 was 0.5, TCP for all plans of the five patients was within 99% in either the planned dose or the real dose. And TCP was almost independent of the clonognic cell density, within 0.1% variation from 10^3 to 10^6 /cm^3. When SF_2 was 0.6, TCP value was patient and N_0 dependent. If the tumor cell density was less than 10^5/cm^3, then the TCP was close to 1 for plans with different margins for each patient. As the cell density increased from 10^5 to 10^6, TCP dropped at various rate for each patient. TCP was between 0.81 and 0.85 for two patients and over 0.9 for the other three patients. For different margin plans, TCP value

varied within 1-3%. Also TCP in the real dose agreed within 5% of the value in the plan for all patients.

Figure 34: TCP vs. N_0 evaluation for all six plans for the five patients. N_0 is in log scale ranging from 10^3 to 10^6. TCP value of six plans was compared against each other to determine the margin effect and the real dose delivery against the plan. Solid lines connecting the data points are used for the visibility only.

There are several randomized clinical trials published to compare hypofractionated and normofractionated radiotherapy (Lukka et al. 2005) (Pollack

et al. 2006) (Yeoh et al. 2006). Due to the nature of the lower α/β ratio of prostate cancer, the hypofractionated radiotherapy can achieve better therapeutic gain since prostate are more sensitive to fractionation than nearby late-responding normal tissues. However, there are still a lot of debates about the α/β value of prostate cancer due to radiobiological uncertainties (Dasu, 2007). Brenner calculated the α/β value 1.5Gy (Brenner and Hall, 1999) which is similar to the value obtained from Fowler (Fowler et al. 2001). Wang et al obtained a value of 3.1Gy (Wang et al. 2003). At the same time, the risk of acute toxicity are increased by reducing the total treatment time. The advantage of using hypofractionation stills needs to be further investigated using randomized trials with better understanding of the α/β value of prostate cancer.

3.3.5 Normal Tissue Evaluation

Rectum and bladder doses were also compared to evaluate the tissue toxicity for each patient. As the margin was reduced from 10 mm to 5/3 mm or from 5/3 mm to 3 mm, rectum and bladder doses were reduced significantly. However, the maximum dose in rectum and bladder were same in the in vicinity of PTV in all scenarios.

Table 13: Dose statistics comparison for rectum between the planned dose and the real dose for three different margin settings

Patient		Plan Dose 10/6	Real Dose 10/6	%Diff	Plan dose 5/3	Real Dose 5/3	%Diff	Plan Dose 3	Real Dose 3	%Diff
1	Min Dose	355	314	-11.5%	236	277	17.4%	206	216	4.9%
	Mean Dose	3355	3892	16.0%	2940	3490	18.7%	3012	3383	12.3%
	Max Dose	8104	8161	0.7%	8069	8154	1.1%	8001	7950	-0.6%
2	Min Dose	243	281	15.6%	189	228	20.6%	186	202	8.6%
	Mean Dose	3697	4546	23.0%	3215	4155	29.2%	2884	3877	34.4%
	Max Dose	8717	8579	-1.6%	8690	8610	-0.9%	8704	8556	-1.7%
3	Min Dose	246	544	121.1%	200	353	76.5%	162	289	78.4%
	Mean Dose	3563	5074	42.4%	2771	4206	51.8%	2669	4153	55.6%
	Max Dose	7828	7811	-0.2%	7805	7797	-0.1%	7840	7717	-1.6%
4	Min Dose	255	257	0.8%	194	197	1.5%	183	176	-3.8%
	Mean Dose	4089	4534	10.9%	3437	3981	15.8%	3055	3656	19.7%
	Max Dose	8337	8204	-1.6%	8267	8214	-0.6%	8277	8216	-0.7%
5	Min Dose	301	443	47.2%	229	313	36.7%	206	260	26.2%
	Mean Dose	4152	4983	20.0%	3360	4340	29.2%	2973	3984	34.0%
	Max Dose	7939	7848	-1.1%	8061	7869	-2.4%	7998	7872	-1.6%

The rectum dose statistics is summarized in table 13 for all 6 plans for five patients. The maximum dose delivered to rectum was at the same level as the planned dose. Different margin plans had similar CTV maximum dose located at the posterior edge, closest to rectum. The mean dose to rectum increased between 10% - 25% for four patients and over 40% for one patient, which had relatively small rectum volume. This analysis showed that margin reduction is a very effective tool in reducing the rectal dose.

Figure 35: Rectum EUD of five patients based on Emami's data where TD_{50}=80Gy, n=0.12, m=0.15. Blue bars represent EUD based on the real dose. Red bars represent EUD based on the planned dose.

EUD and NTCP were calculated to evaluate reaction of rectum to radiation. Rectal EUD in the real delivery and the plan were compared in Fig.35 at the three margin settings. EUD increased 5-7% in the real delivery of plan with 10/5 mm margin for all five patients. As the margin wad reduced, the percent difference increased to 5-14%. For the larger margin, there was more of the rectum volume overlapping with the PTV. Therefore, variations of the rectal dose caused by the deformations were smaller.

NTCP was calculated based on Emami's fitting data to evaluate rectal complication and is shown in Fig.36. Margin reduction from 10/6 mm to 5/3 mm was a very effective way to reduce GI toxicity. NTCP was decreased by 6% on average for each patient. As the margin was further reduced from 5/3 mm to 3mm, NTCP was decreased by 2% on average. Patient 2 showed highest increase of NTCP which was about 10% of the real dose delivery. On average, NTCP was increased by 6% for the real dose relative to the planned dose.

Figure 36: NTCP comparison for rectum between the real dose and the planned dose for the three margin settings. Each figure shows the real NTCP (filled square) vs. the planned NTCP (square). The X-axis shows the value of each margin. Solid lines connecting the data points are used for the visibility only.

Figure 37: NTCP comparison of late rectal bleeding between the real dose and the planned dose for the three margins. Grade 2/3 late bleeding was calculated based on parameters where TD_{50}=81.9Gy, n=0.23, m=0.19. Grade 3 late bleeding was calculated based on parameters where TD_{50}=78.6Gy, n=0.06, m=0.06. Markers with filled square showed NTCP of real grade 2/3 bleeding. Markers with square showed NTCP of planned grade 2/3 bleeding. Markers with filled triangle represented NTCP of real grade 3 bleeding only. Markers with triangle represented NTCP of planned grade 3 bleeding only. Solid lines connecting the data points are used for the visibility only.

Rectal bleeding was also evaluated based on Italian multi-centric data. Both grade 2/3 and grade 3 alone rectal bleedings were estimated and presented in Fig.37. NTCP calculated based on the real dose distribution indicated that the possibility of having rectal bleeding with grade level 2 or 3 was less than 10%.

When the margin was 3 mm, NTCP was about 4% on average of real dose and 1% of planned dose of rectal bleeding. When the margin was 5/3 mm, NTCP was about 6% of the real dose and 2% of the planned dose. When the margin was enlarged to 10/6 mm, NTCP was about 9% of real dose and 4% of planned dose. Patient 2 showed very high risk of bleeding, about 18% for grade 3 level.

Similar biological evaluation was performed for bladder. Emami's data were used for EUD calculation (Fig.38). EUD of the real dose was 3% - 9% higher than that of the planned dose for thes patient 1-3, 11%-20% higher for the patients 4-5. Also, EUD increasing rate showed a negative correlation with margin. As the margin was reduced, the EUD difference became larger. If the same parameters were used for NTCP calculation to evaluate symptomatic bladder contracture, NTCP was zero for all cases. Since bladder dose was relatively low, there was no risk of contracture when the dose for the complication probability of 50% was 80Gy. Not many papers have been published to discuss GU toxicity. There are two reasons. First, the dose volume information was not reliable for bladder which volume had varied significantly between fractions. Second, it took a longer time to follow up late GU toxicity since it increased continuously with time. Data published (TD_{50} =77.6Gy, n=0.00995, m=0.022) by Cheung was used for NTCP calculation to evaluate late GU toxicity with grade equal or greater than 1. Since n was very small, bladder was considered a serial organ. The complication was directly related to the D_{max} of the bladder. NTCP was smaller in the real dose delivery since the real D_{max} was smaller than the planned D_{max}. Patient 3 had almost no complications while the patient 2 had

100% possibility to have GU toxicity greater than grade 1. It was because D_{max} was about 80Gy for the patient 2 and only 74Gy for the patient 3. Smaller margins could not reduce late GU toxicity effectively since D_{max} was at the same magnitude in the bladder no matter which margin was applied.

Figure 38: Bladder EUD of five patients based on Emami's data where TD_{50}=80Gy, n=0.5, m=0.11. Blue bar represented EUD based on real dose. Red bar represented EUD based on planned dose.

Figure 39: NTCP comparison of bladder between the real dose and the planned dose for three margins. Each figure showed real NTCP (filled square) vs. planned NTCP (square). The marker showed the value for each margin. Patient 3 (c) and 5 (e) had very low NTCP, less than 20% for 10mm margin plan. Patient 2 (b) showed almost 100% complication. Patient 1 (a) and 4 (d) were in the middle range level. NTCP of the real dose was higher than that of planned dose. Solid lines connecting the data points are used for the visibility only.

3.3.6 Re-Optimization

There are typically 40-42 treatment fractions to treat prostate cancer. Re-optimization schedule was a tradeoff between the labor intensity and an optimal isodose coverage. On one side, it was not necessary to re-optimize treatment plan at every single fraction since deviation in one fraction was very minimal. On the other side, if the optimization was not performed for several fractions and an OAR received much higher dose than expected, it would be difficult to limit the dose to the OAR in the re-optimization while maintaining the PTV dose coverage.

Schedule for optimization was studied to evaluate the consequences of dose volume effect.

Figure 40: DVH comparison between real dose and planned dose at (a) 5th fraction, (b)10th fraction, (c) 15th fraction, (d)20th fraction, (e) 25th fraction, (f) 30th fraction, (g) 35th fraction, (h) 42nd fraction. The upper DVH lines of rectum and bladder showed the real dose and the lower ones were the planned dose. The discrepancy was accumulated over fractions. PTV and CTV DVH did not have large deviation.

The accumulated dose at every 5th fraction of the real delivery was compared with the planned dose for patient1. DVHs in Fig.40 showed that the target coverage over fractions was very close while the OAR had larger dose deviation. The dose discrepancy at first five fractions was very minimal and it increased significantly at 10th fraction due to larger organ deformation in those treatment fractions. Once the large deviation happened, it would add up and contribute to even larger discrepancy in the following fractions. Re-optimization was necessary then to eliminate overdose of rectum and bladder.

Figure 41: DVH comparison planned dose and accumulated dose at every ten fractions plus re-optimized dose for the remaining fractions. (a) Accumulated dose at 10th fraction plus re-optimized dose of the rest 32 fractions. (b) Accumulated dose at 20th fraction plus re-optimized dose of the rest 22 fractions. (c) Accumulated dose at 30th fraction plus re-optimized dose of the rest 12 fractions. (d) Accumulated dose at 40th fraction plus re-optimized dose of the rest 2 fractions.

Fig. 41 compared the target and the OAR dose after optimization and the planned dose at different optimization schedule. Re-optimization was performed at 10^{th}, 20^{th}, 30^{th}, and 40^{th} fraction to evaluate the effectiveness of limiting the OAR dose while maintaining the target coverage. Reconstructed dose was added to dose of the remaining fractions after the optimization to show the total dose that a patient would receive. It showed that if the plan was re-optimized at 10^{th} (Fig.41 (a)) or 20^{th} fraction (Fig.41(b)), the total doses to the rectum and the bladder were very similar to the planned dose with minor deviations. CTV and PTV coverage was matched with a prescription very well. If the plan was re-optimized at 30^{th} fraction (Fig.41 (c)), since there was a large deviation between the reconstructed dose and the planned dose to OAR, optimization could not limit OAR dose to the original plan with only 12 fractions left. If the re-optimization was conducted at the 40^{th} fraction (Fig.41 (d)), it was impossible to apply optimization in the last 2 fractions. Large deviation of the total dose to bladder and rectum still existed while dose inhomogeneity to PTV was significantly increased due to constraint setting in optimization to reduce OAR dose.

3.4 Conclusion

The development of CBCT has opened a door to a possibility of acquiring a patient's anatomical information in the treatment position. Over the years since CBCT has been used clinically for radiation therapy, the image quality has been improved significantly. Not only can CBCT be used for online patient setup, but it is also demonstrated that CBCT can be used for accurate dose calculation at certain sites like prostate. DIR has also been studied at multiple institutions and

used for clinical evaluation of patient treatments. Even though DIR of CBCT images is still a challenging task, especially for the prostate site, this study validates that CBCT images can be reliably fused with helical CT images with a proper patient bowel preparation. Three methods are used to evaluate the image registration results quantitatively and qualitatively. With the tools of CBCT and DIR, the next generation of radiation treatment – ART has emerged to reduce treatment uncertainties.

IGRT can effectively assess intra-, inter-fraction motion of target with different imaging modalities. However, it cannot compensate for dosimetric consequences. The strategy of ART in this study is to (1) calculate dose on each CBCT set to know the real dose delivery (2) deform CBCT images to SIM CT images (3) re-construct the dose based on a transformation matrix generated from DIR (4) re-optimize a patient plan if necessary. With ART, the treatment delivery precision can be enhanced even over eight weeks' treatment periods. Five patients with prostate cancer have been studied retrospectively under IRB approved protocol. Different evaluation methods such as DVH, isodose lines, and radiobiological model were applied to compare the reconstructed dose and the planned dose.

The reason to use ART was that prostate position and shape varies daily mainly due to rectal and bladder filling. MD Anderson study showed that the local control rate could be reduced by about 25% in distended rectum patients compared to empty rectum (Crevoisier et al 2005). Such clinical evidence confirmed the importance of targeting prostate precisely during both the planning

and the treatment. However, IGRT along could perform such targeting. Several studies have shown that TCP can be improved 5-10% with IGRT. In our study, ART did not show the improvement of TCP if the patient was setup with CBCT. However, EUD of rectum and bladder was increased a lot due to tissue deformation, which varies daily. NTCP of rectum was increased by 6% on average in the reconstructed dose. Grade 2 and grade 2/3 rectal bleeding were also evaluated based on the reconstructed dose for each patient. There was no difference in bladder complications between the planned dose and the reconstructed dose since late GU toxicities depend mainly on D_{max}.

With the advantage of ART, CTV margins could be further reduced to preserve critical organs surrounding the target. Two different margins 5/3 mm and 3mm were used in re-planning to determine the effectiveness of margin reduction. TCPs were within 3% among all three margins for each patient. However, small margin could reduce dose to OAR significantly. NTCP of rectum was reduced by 6% with 5/3 mm margin plan and 8% with 3mm margin plan. Late GU toxicity remains the same since D_{max} was at same magnitude in each margin plan.

Re-optimization schedule was also studied to achieve a tradeoff between the labor intensity and an ideal treatment. The common sense to re-optimize at the last fraction was not applicable in reality since if the rectum and the bladder were overdosed already, there was no way to push dose back to the planned dose. And target dose would be very inhomogeneous if the hard dose limiting constraints were imposed on the OAR. On the other hand, there was no

necessity to re-optimize at each single treatment since dose deviation was not significant. Re-optimization schedule was compared at 10^{th}, 20^{th}, 30^{th}, and 40^{th} fraction. It was recommended to re-optimize treatment plan at every 10^{th} fraction. ART has a potential to improve the local control rate and to reduce toxicity. It also correlates the actually delivered dose to the clinical outcomes, which brings a more direct clinical relevance than the conclusions drawn in the published data based on the planning dose distribution. Even though it is still in the early stages and there are not many data on the issue, ART is definitely a promising treatment strategy to improve the fight against cancer.

CHAPTER 4: SUMMARY AND FUTURE WORK

CBCT provides volumetric information for daily target localization. Such detailed anatomical information can be compared with a treatment plan CT online to adjust for setup errors. It is highly beneficial for the treatment of prostate cancer over an eight week course of treatment. CBCT can be used to align the prostate which cannot be otherwise visualized in 2D imaging. Also, bladder and rectum information can be acquired for a clinical judgment before each treatment. The experience of CBCT is very encouraging for soft tissue localization. However, since CBCT has to be acquired for each fraction, the accumulated dose can be much higher than that of a diagnostic CT. Future, relative biological effectiveness (RBE) value of the KV is still under investigation. Dose delivered from CBCT should be well understood to be used in the clinic.

The doses to skin and in phantom are measured with a pelvis rando phantom and CIRS phantom using TLD and ion chamber, following the AAPM TG61 protocol. CBCT dose over a treatment course of 42 fractions is about 1Gy at center, 2Gy at skin and 4Gy to a femoral head. It is much smaller than the prescription dose to the target and dose to the peripheral regions. Considering the advantage of eliminating the patient setup uncertainty, CBCT provides a powerful tool to improve a patient treatment. CBCT images can also be used for the post treatment verification of dosimetric effects. ART framework has been established to advance the treatment precision to the next level. Dose calculation accuracy on CBCT, DIR, radiobiological model and re-optimization schedule are addressed carefully. The study has shown that ART can help to better

understand the real dose delivery to patients and further reduce the normal tissue toxicity.

However, there are still some issues with CBCT and ART that need to be resolved. The image quality of CBCT needs to be further improved. With a large scatter contribution, it is difficult to distinguish and delineate internal organs on a CBCT. With dose reduction techniques that are limiting projection data, the poor image quality is even more pronounced. Scatter radiation can also cause HU non-linearity which degrades the accuracy of dose calculations on CBCT. Also poor image quality reduces the precision of DIR which produces an additional uncertainty for dose reconstruction. Scatter reduction techniques need to be developed to improve CBCT image quality.

It takes several hours to register one CBCT set to SIM-CT using B-Spline DIR. Thus it is not feasible to apply it clinically. GPU (graphics processing unit) is more effective than CPU for DIR with highly parallel structures. The fusion time can be significantly reduced with GPU based DIR. A faster and more accurate DIR algorithm needs to be integrated for ART.

DIR has been evaluated with multiple methods. Verification with implanted seeds cannot represent the registration result for the whole volume. Reviewing images slice by slice is very time consuming and is subjective due to observer variability. UE shows its potential to validate DIR quantitatively and qualitatively with an automated algorithm. However, it is still in the early stage of development. Future efforts and QA are needed to release it for clinical use.

There are many publications discussing radiobiological model for the prediction of radiotherapy outcome. However, there are still a lot of uncertainties to involve in using such a radiobiological model. Prostate α/β ratio is still under debate. TCP and NTCP parameters generated by curve fitting from multiple institutions are not applicable universally. There are still implements to using radiobiological models as a standard tool to evaluate treatment plans.

ART has also opened the road for hypofractionation. Different hypofractionated schemes have been activated for prostate cancer treatment. They vary from 2.3 Gy/fraction in 28 fractions up to 8Gy in 5 fractions. However due to current limits on DIR and CBCT image quality, it is hard to distinguish prostate and rectal wall with good registration. So it is difficult to escalate the dose to very high levels since a small portion of rectal wall may overlap with PTV and receive the same dose, which could lead to severe complications, like bleeding and fissures. The strategy should focus on limiting dose to the overall PTV-rectal wall region in order to escalate the prescription dose to prostate.

ART can also be applied to other treatment sites such as lung and Head and Neck (H&N) etc. However, the current CBCT images of lung scan are poor due to motion artifacts and scatter. Neither can it be used for DIR nor it can achieve accurate dose calculation. 4D-CBCT with scatter correction needs to be developed and evaluated in order to implement ART for lung cancer.

IMRT has been used for the treatment of H&N cancer extensively in the past decade to preserve the surrounding critical organs with high conformality to the tumor. However, the dose gradients are very sharp in the H&N plan for organ

sparing. Due to the long treatment period (~2 month), the variability of patient setup and anatomy change due to weight loss or tumor shrinkage can lead to significant dosimetric changes. Ballivy et al. scanned eight H&N patients weekly and found out the contralateral parotid and spinal cord dose were higher than originally planned. ART can be an effective treatment strategy to discover any detriment to target coverage and overdose to the critical organs with patient's anatomic change. The margin reduction and optimization schedule can also be investigated using the framework developed.

REFERENCES

1. Alaei P, Gerbi B J, and Geise R A, "Evaluation of a model-based treatment planning system for dose computations in the kilovoltage energy range." *Med. Phys* 27 (2000): 2821-6.
2. Alaei P, Gerbi B J, and Geise R A, "Generation and use of photon energy deposition kernels for diagnostic quality x-rays." *Med. Phys* 26 (1999): 1687-97.
3. Alaei P, Gerbi B J, and Geise R A, "Lung dose calculations at kilovoltage x-ray energies using a model-based treatment planning system." *Med. Phys.*, 2001: 194-8.
4. Ballivy O, Parker W, Vuong T and et al., "Impact of geometric uncertainties on dose distribution during intensity modulated radiotherapy of head-and neck cancer: The need for a planing target volume and a planning organ-at-risk volume." *Curr Oncol* 13 (2006): 108-15.
5. Beard C J, Kijewski P, Bussiere M, and et al., "Analysis of prostate and seminal vesicle motion: Implications for treatment planning." *Int J Radiat Oncol Biol Phys* 34 (1996): 451-58.
6. Bhat M, Pattison J, Bibbo G, and Cao M, "Off-axis x-ray spectra: a comparison of Monte Carlo simulated and computed x-ray spectra with measured spectra." *Med. Phys.* 26 (1999): 303-9.
7. Brenner, D J and Hall E J, "Fractionation and protraction for radiotherapy of prostate carcinoma." *Int J Radiat Oncol Biol Phys* 43 (1999): 1095–1101
8. Brenner D J, "Is it time to retire the CTDI for CT quality assurance and dose optimization?" *Med. Phys.* 32 (2005): 3225-6.

9. Brenner, D J, Martinez A A, Edmundson G K, and et al., "Direct evidence that prostate tumors show high sensitivity to fractionation (low alpha/beta ratio), similar to late-responding normal tissue." *Int J Radiat Oncol Biol Phys* 52 (2002): 6–13

10. Burman C, Kutcher G J, and Goitein B, Emami M, "Fitting of normal tissue tolerance data to an analytic function." *Int. J. Radiat. Oncol., Biol. Phys.* 21 (1991): 123-35.

11. Cheung Rex, Tucker S L, and Lei D, "Investigation of bladder dose and volume factors influencing late urinary toxicity after external beam radiotherapy for prostate." *Int J Radiat Oncol Biol Phys.* 67 (2007): 1059-65.

12. Coudin D, Ginette, and Marinello, "Lithium borate TLD for determining the backscatter factors for low-energy x-rays: Comparison with chamber-based and Monte Carlo derived values." *Med. Phys.* 25 (1998): 347-53.

13. Craig T, Brochu D, and Vandyk J, "A quality assurance phantom for three-dimensional radiation treatment planning." *Int. J. Radiat.Bio. Phy.* 44 (1999): 955-66.

14. Crevoisier R, Tucker S, Dong L, and et al., "Increased risk of biomedical and local failure in patients with distended rectum on the planning CT for prostate cancer radiotherapy." *Int. J. Radiat.Bio. Phy.* 62 (2005): 965-73.

15. Dasu A, "Is the alpha/beta value for prostate tumours low enough to be safely used in clinical trials?" *Clin Oncol* 19 (2007): 289-301.

16. Dawson L A, Mah K, Franssen E, and et al., "Target position variability throughout prostate radiotherapy." *Int J Radiat Oncol Biol Phys* 42 (1998): 1155-61.

17. Ding G X, Duggan D M, and Coffey C W, "Accurate patient dosimetry of kilovoltage cone-beam CT in radiation therapy." *Med. Phys.* 35 (2008): 1135-44

18. Ding George, et al., "A study on adaptive IMRT treatment planning using kV cone-beam CT." *Radiotherapy and Oncology* 85 (2007): 116-25.

19. Dixon R L, "A new look at CT dose measurement: beyond CTDI." *Med. Phys.* 30 (2003): 1272-80.

20. Emami B., et al., "Tolerance of normal tissue to therapeutic radiation." *Int. J. Radiat. Oncol., Biol., Phys* 21 (1991): 109-22.

21. Fowler J F, and Chappell M A, Ritter R T, "Why hypofractionated protocols should be tested for prostate cancer?" *Int J Radiat Oncol Biol Phys* 56 (2003): 1093-1104.

22. Fowler J F, Chappell R, Ritter M, "Is a/b ratio for prostate tumors really low? " *Int J Radiat Oncol Biol Phys* 50 (2001):1021–31.

23. Guan H, and Dong H, "Dose calculation accuracy using cone-beam CT (CBCT) for pelvic adaptive radiotherapy." *Phys. Med. Biol.* 54 (2009): 1-12.

24. Ioppolo J L, Price R I, Tuchyna T, and Buckley C E, "Diagnostic x-ray dosimetry using Monte Carlo simulation." *Phys. Med. Biol.* 47 (2002): 1707-20.

25. Islam M K, et al., "Patient dose from kilovoltage cone beam computed tomography imaging in radiation therapy." *Med. Phys.* 33 (2006): 1573-82.

26. Jones A K, Pazik F D, Hintenlang D E, and Bolck W E, "MOSFET dosimeter depth-dose measurements in heterogeneous tissue-equivalent phantoms at diagnostic x-ray energies." *Med. Phys.* 32 (2005): 3209-13.
27. Klein S, and Staring M, "Elastix Manual." 2008.
28. Lester H, and Arridge S R, "A survey of hierarchical non-linear medical image registration." *Pattern Recognit* 32 (1999): 129-49.
29. Luis L, Will S, Lydia N, and Josh C, "The ITK Software Guide." 2005.
30. Lukka H, Hayter C, Julian J A et al., "Randomized trial comparing two fractionation schedules for patients with localized prostate cancer." *J. Clin. Oncol.* 23 (2005): 6132-38.
31. Ma C-M, and Seuntjens J P, "Mass-energy absorption coefficient and backscatter factor ratios for kilovoltage x-ray beams." *Phys. Med. Biol.* 44 (1999): 131-43.
32. Ma C-M, et al., "AAPMprotocol for 40–300 kV x-ray beam dosimetry in radiotherapy and radiobiology." *Med. Phys.* 28 (2001): 868-93.
33. Marks L B, et al., "Use of normal tissue complication probability models in the clinic?" *Int J Radiat Oncol Biol Phys* 76 (2010):S10–19.
34. Martinez A, Vargas C, Kestin L, and et al., "Interim results of a Phase II dose escalating trial with image guided adaptive radiotherapy for the treatment of early of high risk prostate cancer patients: Improved outcome with increased EBRT dose." 63 (2005): S305-6.
35. Omrane B, Verhaegen F, Chahed, N and Mtimet S, "An investigation of entrance surface dose calculations for diagnostic radiology using Monte Carlo simulations and radiotherapy dosimetry formalisms." *Phys. Med. Biol.* 48 (2003): 1809-24.

36. Palm A, Nilsson E, and Herrnsdorf, "Absorbed dose and dose rate using the Varian OBI 1.3 and 1.4 CBCT system" *J Appl Clin Med Phys* 11 (2010):229–40

37. Peeters S, Heemsbergen W D, Koper P, and et al. "Dose response in radiotherapy for localized prostate cancer: Results of the Dutch multicenter randomized phase III trial comparing 68 Gy with 78 Gy." *J Clin Oncol* 24 (2006): 1990-96.

38. Pluim J P, and Viergever J B A, Maintz M A, "Mutual-Information-Based Registration of Medical Images: A Survey." *IEEE Transactions on Medical Imaging* 22 (2003): 986-1004.

39. Pollack A, Horwitz E M, Feigenberg S J, and et al., "Dosimetry and preliminary acute toxicity in the first 100 men treated for prostate cancer on a randomized hypofractionation dose escaliation trial." *Int J Radiat Oncol Biol Phys* 64 (2006): 518-526.

40. Pollack A, Zagars G K, Starkschall G, and et al., "Prostate cancer radiation dose response: Results from the M.D. Anderson phase III randomized trial." *Int J Radiat Oncol Biol Phys* 53 (2002): 1097-1105.

41. Rancati T, Fiorino C, and Gagliardi G, "Fitting late rectal bleeding data using different NTCP models: results from an Italian multi-centric study (AIROPROS0101)." *Radiother Oncol* 73 (2004): 21-32.

42. Roeske J C, Forman, J D and Mesina C F, and et al., "Evaluation of changes in the size and location of the prostate, seminal vesicles, bladder, and rectum during a course of external beam radiation therapy." *Int J Radiat Oncol Biol Phys*, 1995: 1321-29.

43. Sanchez-Nieto B, and Nahum A E, "The delta-TCP concept: a clinically useful measure of tumor control probability." *Int J Radiat Oncol Biol Phys* 44 (1999): 369-80.

44. Schallenkamp J M, Herman M G, Kruse J J, and Pisansky T M, "Prostate position relative to pelvic bony anatomy based on intraprostatic gold markers and electronic portal imaging." *Int. J. Radiat. Oncol. Biol.* 65 (2005): 800-11.

45. Thirion J P, "Image matching as a diffusion process: an analogy with Maxwell's demons." *Med Image Anal* 2 (1998): 243-60.

46. Tinger A, Michalski J M, Cheng A, and et al., "A critical evaluation of the planning target volume for 3D conformal radiotherapy of prostate cancer." *Int J Radiat Oncol Biol Phys* 42 (1998): 213-21.

47. Wang J Z, Guerrero M, and Li X A, "How low is the alpha/beta ratio for prostate cancer." *Int J Radiat Oncol Biol Phys* 55 (2003): 194-203.

48. Webb S, "Optimum parameters in a model for tumor control probability including interpatient heterogeneity." *Phys Med Biol* 39 (1994): 1895-1914.

49. Webb S, and Nahum A E, "A model for calculating tumour control probability in radiotherapy including the effects of inhomogeneous distributions of dose and clonogenic cell density." *Phys. Med. Biol.* 38 (1993): 653-66.

50. Xing L, Siebers J, Keall P, "Computational challenges for image guided radiation therapy: framework and current research." *Semin Radiat Oncol* 17 (2007): 245-57.

51. Yang Y E, Schreibmann T, Wang C, and Xing L, "Evaluation of on-board KV cone beam CT (CBCT)-based dose calculation." *Phys. Med. Biol.* 52 (2007): 685-705.

52. Yeoh E E, Holloway R H, Fraser, "Hypofractionated versus conventionally fractionated radiation therapy for prostate carcinoma: updated results of a phase III randomized trial." *Int. J. Radiation Oncology Biol. Phys.* 66 (2006): 1072-83.

53. Yoo Sua, and fang-fang Yin, "Dosimetric feasibility of Cone-Beam CT-Based treatment planning compared to CT-Based treatment planning." *Int. J. Radiation Oncology Biol. Phys.* 66 (2006): 1553-61.

54. Zelefsky M J, Crean D, Mageras G S, and et al., "Quantification and predictors of prostate position variability in 50 patients evaluated with multiple CT scans during conformal radiotherapy." *Radiother Oncol* 50 (1999): 225-34.

55. Zelefsky M J, Leibel S A, Gaudin P B, and et al., "Dose escalation with three-dimensional conformal radiation therapy affects the outcome in prostate cancer." *Int J Radiat Oncol Biol Phys* 41 (1998): 491-500.

56. Zerda A, Armbruster B, and Xing L, "Formulating adaptive radiation therapy (ART) treatment planning into a closed-loop control framework." *Phys. Med. Biol.* 52 (2007): 4137-53.

57. Zhong H, Kim J, and Chetty I, "Analysis of deformable image registration accuracy using computational modeling." *Med. Phys.* 37 (2010): 970-79.

58. Zhong H, Peters T, and Siebers J, "FEM based evaluation of deformable image registration in radiation therapy." *Phys. Med. Biol* 52 (2007): 4721-38.

ABSTRACT

ADAPTIVE RADIATION THERAPY OF PROSTATE CANCER

by

NING WEN

August 2010

Advisor: Dr. Teamour Nurushev

Major: Medical Physics

Degree: Doctor of Philosophy

ART is a close-loop feedback algorithm which evaluates the organ deformation and motion right before the treatment and takes into account dose delivery variation daily to compensate for the difference between planned and delivered dose. It also has potential to allow further dose escalation and margin reduction to improve the clinical outcome. This retrospective study evaluated ART for prostate cancer treatment and radiobiological consequences. An IRB approved protocol has been used to evaluate actual dose delivery of patients with prostate cancer undergoing treatment with daily CBCT.

The dose from CBCT was measured in phantom using TLD and ion chamber techniques in the pelvic scan setting. There were two major findings from the measurements of CBCT dose: (1) the lateral dose distribution was not symmetrical, with Lt Lat being ~40% higher than Rt Lat and (2) AP skin dose varies with patient size, ranging 3.2-6.1 cGy for patient's AP separation of 20-33 cm (the larger the separation, the less the skin dose) but lateral skin doses depend little on separations.

Five low risk localized prostate cancer patients were selected for the study. The CTV included prostate and 1cm proximal seminal vesicle. PTV was created by adding 1 cm margin to CTV except 6 mm posteriorly to limit rectal dose. The treatment plans were 7 to 9 fields IMRT. CBCT was acquired before each treatment for online image guidance. The rigid registration was performed online to fuse CBCT to SIM-CT. The patient position was corrected in three translational directions based on registration results.

Dose was recalculated on each CBCT set under the same treatment plan. DIR was performed between SIM-CT and evaluated for each CT sets. Dose was reconstructed and accumulated to reflect the actual dose delivered to the patient. Then the adaptive plans were compared to the original plan to evaluate tumor control and normal tissue complication using radiobiological model. Different PTV margins were also studied to access margin reduction techniques. If the actual dose delivered to the PTV deviated significantly from the prescription dose for the given fractions or the OAR received higher dose than expected, the treatment plan would be re-optimized based on the previously delivered dose. The optimal schedule was compared based on the balance of PTV dose coverage and inhomogeneity, OAR dose constraints and labor involved.

DIR was validated using fiducial marker position, visual comparison and UE. The mean and standard deviation of markers after rigid registration in L-R direction was 0 and 1 mm. But the mean was 2-4 mm in the A-P and S-I direction and standard deviation was about 2 mm. After DIR, the mean in all three directions became 0 and standard deviation was within sub millimeter. UE

images were generated for each CT set and carefully reviewed in the prostate region. DIR provided accurate transformation matrix to be used for dose reconstruction.

The delivered dose was evaluated with radiobiological models. TCP for the CTV was calculated to evaluate tumor control in different margin settings. TCP calculated from the reconstructed dose agreed within 5% of the value in the plan for all patients with three different margins. EUD and NTCP were calculated to evaluate reaction of rectum to radiation. Rectal EUD increased 5-7% in the real delivery of the plan with 10/5 mm margin for all five patients. As the margin was reduced, the percent difference increased to 5-14%. Margin reduction from 10/6 mm to 5/3 mm was a very effective way to reduce predicted GI toxicity. Calculated NTCP was decreased by 6% on average for each patient. As the margin was reduced from 5/3 mm to 3mm, NTCP was decreased by 2% on average. NTCP calculated based on actual dose distribution indicated that possibility was less than 10% to have rectal bleeding with grade level 2 or 3. Similar biological evaluation was performed for bladder. EUD of actual dose was 3% - 9% higher than that of planned dose of patient 1-3, 11%-20% higher of patient 4-5. Smaller margins could not reduce late GU toxicity effectively since bladder complication was directly related to D_{max} which was at the same magnitude in the bladder no matter which margin was applied.

Re-optimization was performed at the 10^{th}, 20^{th}, 30^{th}, and 40^{th} fraction to evaluate the effectiveness to limit OAR dose while maintaining the target coverage. Reconstructed dose was added to dose from remaining fractions after

optimization to show the total dose patient would receive. It showed that if the plan was re-optimized at 10th or 20th fraction, total dose to rectum and bladder were very similar to planned dose with minor deviations. If the plan was re-optimized at the 30th fraction, since there was a large deviation between reconstructed dose and planned dose to OAR, optimization could not limit the OAR dose to the original plan with only 12 fractions left. If the re-optimization was done at the 40th fraction, it was impossible to compensate in the last 2 fractions. Large deviations of total dose to bladder and rectum still existed while dose inhomogeneity to PTV was significantly increased due to hard constraints set in the optimization to reduce OAR dose.

In summary, ART did not show improvements in TCP if the patient was setup with CBCT. However, EUD of rectum and bladder was increased significantly due to tissue deformation which varied daily. With the power of ART, margins added to the CTV could be further reduced to preserve critical organs surrounding the target.

AUTOBIOGRAPHICAL STATEMENT

NING WEN

Education

B.S. – Physics (2002), Lanzhou University, Lanzhou, China
M.A. – Physics (2004), Wayne State University, Detroit, MI, USA
M.S. – Medical Physics (2006), Wayne State University, Detroit, MI, USA
Ph.D. – Medical Physics (2010), Wayne State University, Detroit, MI, USA
M.B.A. – Stephen M. Ross School of Business (2011), University of Michigan, Ann Arbor, MI, USA

Professional Positions:

2009-Present Senior Staff Physicist, Henry Ford Health System, Detroit, MI
2008-Present Clinical Assistant Professor, Wayne State University, Detroit, MI
2007-2009 Senior Associate Physicist, Henry Ford Health System, Detroit, MI
2006-2007 Junior Medical Physicist, Oncure Medical Corp., Modesto, CA
2005-2006 Medical Physicist (Intern), Henry Ford Health System, Detroit, MI
2005 Reach Assistant, Wayne State University, Detroit, MI
2003-2005 Teaching Assistant, Wayne State University, Detroit, MI

Board Certification / Professional Memberships

2009-Present Diplomate, American Board of Radiology
2009-Present Member, American Society for Therapeutic Radiology and Oncology
2006-Present Member, American Association of Physicists in Medicine

Selected Honors and Awards

2008-2010 Graduate-Professional Scholarships, Wayne State University
2002 Graduation with high distinction, Lanzhou University
1998-2002 Fellowship, Lanzhou University

Selected Peer-Reviewed Publications

- N Wen, H Guan, R Hammoud, D Pradhan, T S Nurushev, Q Chen, S Li, B Movsas, "Dose delivered from Varian's CBCT to patients receiving IMRT for prostate cancer", Phys. Med. Biol. 52(2007) 2267–2276
- J Jin, L Ren, Q Liu, J Kim, N Wen, H Guan, B Movsas, I Chetty, "Simultaneous scatter reduction and correction to improve image quality in Cone-Beam Computed Tomography (CBCT)", Med. Phy., submitted in Dec 2009
- H Guan, N Wen, Y Xu, "Measurement of cone beam CT dose delivered to head scan using Gafchromic XR-QA films and a flatbed scanner", Phys. Med. Biol., submitted in Feb 2010
- M Fragoso, N Wen, S Kumar, D Liu, S Ryu, B Movsas, M Ajlouni, I Chetty, "Dosimetric verification and clinical evaluation of a new commercial Monte Carlo-based algorithm for application in stereotactic body radiotherapy (SBRT) treatment planning", Phys. Med. Biol. 55 (2010) 4445-4464